University of BRISTOL

School of Chemistry

Fabrication of Black Diamond and Polymer Surfaces for Antimicrobial Applications

Amarita Kaur Chahal

This thesis is submitted in partial fulfilment of the requirements for the Honours Degree of MSci Chemistry at the University of Bristol

Supervisor: Professor Paul May

Second Assessor: Professor Wuge Briscoe

Physical and Theoretical Chemistry

Statement of Limiting Factors

The HFCVD reactor was unable to be used for approximately five weeks. This was primarily due to maintenance in the lab, including the replacement of the extract fan lines. This resulted in delays regarding the diamond substrate growth process.

There were delays in receiving the silicon nanohole substrates from the physics cleanroom which constrained the research time. Consequently, only a single polymer replication could be completed within the project's duration.

Abstract

The rise in antimicrobial resistance (AMR) presents an escalating danger to global public health. This has led to a remarkable growth in research efforts investigating inherently antimicrobial materials that function via a mechanical mechanism rather than existing chemical mechanisms.

This report details the fabrication and characterisation of numerous surfaces for antimicrobial efficacy testing. Black diamond. (bD) and flat diamond (Flat-D) were successfully synthesised via hot filament chemical vapour deposition (HFCVD). Laser Raman spectroscopy confirmed the quality of polycrystalline diamond growth on black silicon and flat silicon wafers, confirming the presence of the characteristic sp^3 crystalline peak at 1332 cm^{-1}. Additionally, scanning electron microscopy (SEM) verified the conformal coating of the nanopillars, achieving an average pillar height of 3.7 μm.

To address the scalability constraints of diamond, we developed a novel soft lithography replication method using NOA-81. As only one polymer replication process was completed, these findings are a preliminary proof-of-concept. While SEM analysis revealed successful fabrication of nanopillar arrays from silicon nanohole templates, isolated areas of the substrate remained unreplicated. This suggests that while NOA-81 is a viable polymer for biomimetic fabrication, the replication process requires further anti-adhesive optimisation to ensure complete pattern transfer.

Preliminary antimicrobial testing against *Escherichia coli* was carried out at the University of Groningen in the Netherlands. Results indicated that all diamond-based surfaces exhibited reduced bacterial adhesion compared to flat silicon, which exhibited the highest level of bacterial attachment. Specifically, the lower adhesion observed on H-terminated bD exhibited a ~ 44% reduction in bacterial adhesion compared to O-terminated samples (1.07×10^7 vs 1.92×10^7 CFU cm^{-2}). This corroborates previous research suggesting that hydrophobic states enhance antimicrobial performance. However, as the Flat-D control unexpectedly exhibited the lowest overall adhesion (7.28×10^6 CFU cm^{-2}), the exact significance of these results is still inconclusive and requires further antimicrobial testing.

Acknowledgements

First and foremost, I would like to thank my project supervisor, Professor Paul May, for the opportunity to work within the diamond lab. His expertise, support, and guidance have been invaluable throughout this process. Secondly, I would like to extend my sincere thanks to Professor Wuge Briscoe for his support and insights throughout the duration of this project.

I would also like to thank Gulnur Zulpukarova for constantly answering my questions and for her supervision around the lab; I wish her the very best for the remainder of her PhD.

Furthermore, a special thank you to the entirety of the BUDGie group for being so welcoming and supportive. Working alongside everyone was an immensely enjoyable experience.

Finally, I would like to say a massive thank you to my Mum and Dad (and dog, Rocco) for their endless love and support throughout the course of my degree. I couldn't have done it without them.

Table of Contents

List of Tables

List of Figures

Acronyms

ABR	Antibiotic Resistance
AMR	Antimicrobial Resistance
ATP	Adenine Triphosphate
bD	Black Diamond
bSi	Black Silicon
CFU	Colony Forming Units
CLSM	Confocal Laser Scanning Microscope
CVD	Chemical Vapour Deposition
E. coli	*Escherichia coli*
EBL	Electron Beam Lithography
EPS	Extracellular Polymeric Substances
Flat-D	Flat Diamond
HAIs	Healthcare-Associated Infections
HFCVD	Hot-Filament Chemical Vapour Deposition
HGT	Horizontal Gene Transfer
ICP-RIE	Inductively Coupled Plasma Reactive Ion Etching
IHME	Institute for Health Metrics and Evaluation
MOF	Metal-Organic Framework
MPCVD	Microwave Plasma Chemical Vapour Deposition
MRSA	Methicillin-Resistant *Staphylococcus aureus*
NIL	Nanoimprint Lithography
NOA-81	Norland Optical Adhesive 81
PBS	Phosphate Buffered Saline
PDMS	Poly (dimethyl siloxane)
PECVD	Plasma-Enhanced Chemical Vapour Deposition
PI	Propidium Iodide
PMMA	Polymethyl Methacrylate
RIE	Reactive-Ion Etching
RLU	Relative Light Units

RMS	Root Mean Square
ROS	Reactive Oxygen Species
SEM	Scanning Electron Microscopy
T_g	Glass Transition Temperature
TMCS	Trimethylchlorosilane
TSB	Tryptic Soya Broth
UVO	UV/Ozone
VRE	Vancomycin-Resistant Enterococci
WCA	Water Contact Angle
ZnONPs	Zinc Oxide Nanoparticles

1. Introduction

1.1 The Global Rise of Antimicrobial Resistance

1.1.1 Antibiotic Resistance

Since the discovery of antibacterial drugs around 80 years ago, antimicrobial resistance (AMR) has evolved into an increasing danger to global public health.[1] A study by the Institute for Health Metrics and Evaluation (IHME) and Oxford University, shows that AMR has been responsible for over 36 million fatalities since 1990, and is predicted to cause 39 million more between 2025 and 2050 if no further policy interventions take place.[2]

AMR stems from microorganisms, including bacteria, viruses, fungi, and parasites, that exhibit continued viability and growth despite exposure to antimicrobial drugs. In bacteria, this phenomenon is known as antibiotic resistance (ABR). Their continued viability and growth can be attributed to the overuse or misuse of these drugs, commonly antibiotics, by humans.

Resistance is broadly classified as either intrinsic or acquired. Intrinsic resistance is an innate characteristic of a bacterial species to naturally resist a particular drug due to the bacteria's structural or functional properties. In contrast, acquired resistance occurs through two principal genetic mechanisms: spontaneous mutation or the acquisition of new genetic material, often via horizontal gene transfer (HGT), which is the non-sexual transfer of genetic material.[3]

There are behaviour-dependent and material-intrinsic solutions to the problem of ABR. For example, during the COVID-19 pandemic it became increasing important to implement behavioural interventions such as handwashing, which relies on human compliance making it episodic. In contrast, physical or intrinsic antimicrobial surface properties provide continuous protection, and are therefore more valuable as they do not require constant human intervention to maintain sterility.

1.1.2 Bacterial Cell Structure

A primary example of intrinsic resistance is the fundamental structural difference between bacterial cell walls (see Figure 1.1). Bacteria can be classified as Gram-positive or Gram-negative, based on the thickness of their cell wall, and their staining properties using a crystal violet-iodine complex and a safranin counter stain. Gram positive bacteria, which have historically been the subject of most reported studies, stain violet or purple and possess a thick (40-80 nm) peptidoglycan layer-consisting of two amino sugars with no outer lipid membrane.[4] In contrast, Gram-negative bacteria do not retain the primary stain and are instead coloured by the pink safranin counterstain.[5] They have a thin (7-8 nm) peptidoglycan layer which is then surrounded by a protective outer lipid membrane.[4] The outer membrane is a key structural feature that is joined to the inner membrane by lipoproteins. Due to the thicker peptidoglycan layer of Gram-positive bacteria, they are often unaffected by physical stress.[6] In spite of this, Gram-negative bacteria have a higher resistance to antibiotics which results in them being accountable for 10-23% of infections, even though they are more susceptible to mechanical rupture.[7]

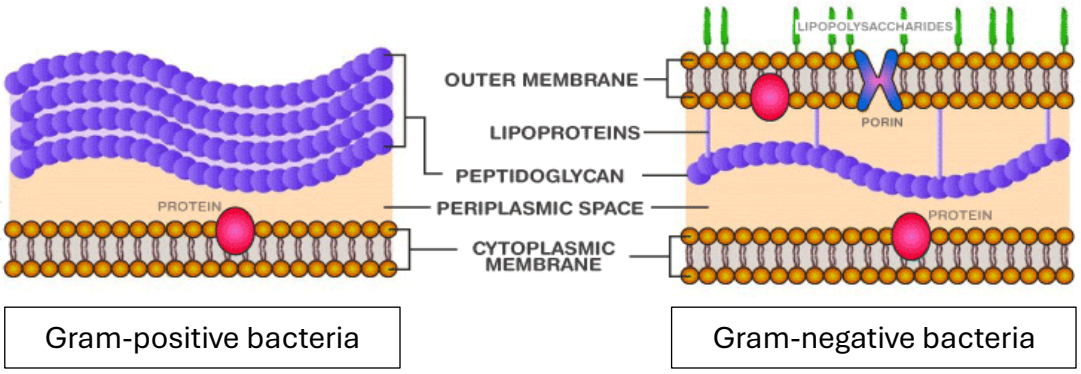

Figure 1.1. Comparative diagram of the cell wall composition of Gram-negative and Gram-positive bacterial cells.[8]

Hence, the diminishing efficacy of traditional chemical methods has created a pressing need for innovative strategies to combat pathogenic bacteria, particularly in clinical environments where healthcare-associated infections (HAIs) are prevalent. Advancement in this field would also translate to tangible benefits in everyday life, affecting commonly touched surfaces, such as door handles, mobile phones and taps.[9] This has led to a paradigm shift, moving from chemical-based techniques to those founded on physical, mechanical principles.

1.1.3 Bacterial Adhesion and Biofilm Formation

Biofilms are microbial aggregates that adhere to an inert substrate, multiply, and are then enclosed within a self-produced and protective matrix of extracellular polymeric substances (EPS) (see Figure 1.2), with matured biofilms being notoriously difficult to eradicate.[10] This leads to biofilm matrixes demonstrating a 10-to-1,000-fold increase in AMR compared to their free floating state.[11] Biofilm formation is important as it is the primary vector for the transmission of infections (attributed to 80% of infections), particularly those related to medical implants.[12] They also have the potential to infect food-contact surfaces, pipelines, heat exchangers, and maritime vehicles.[13–16]

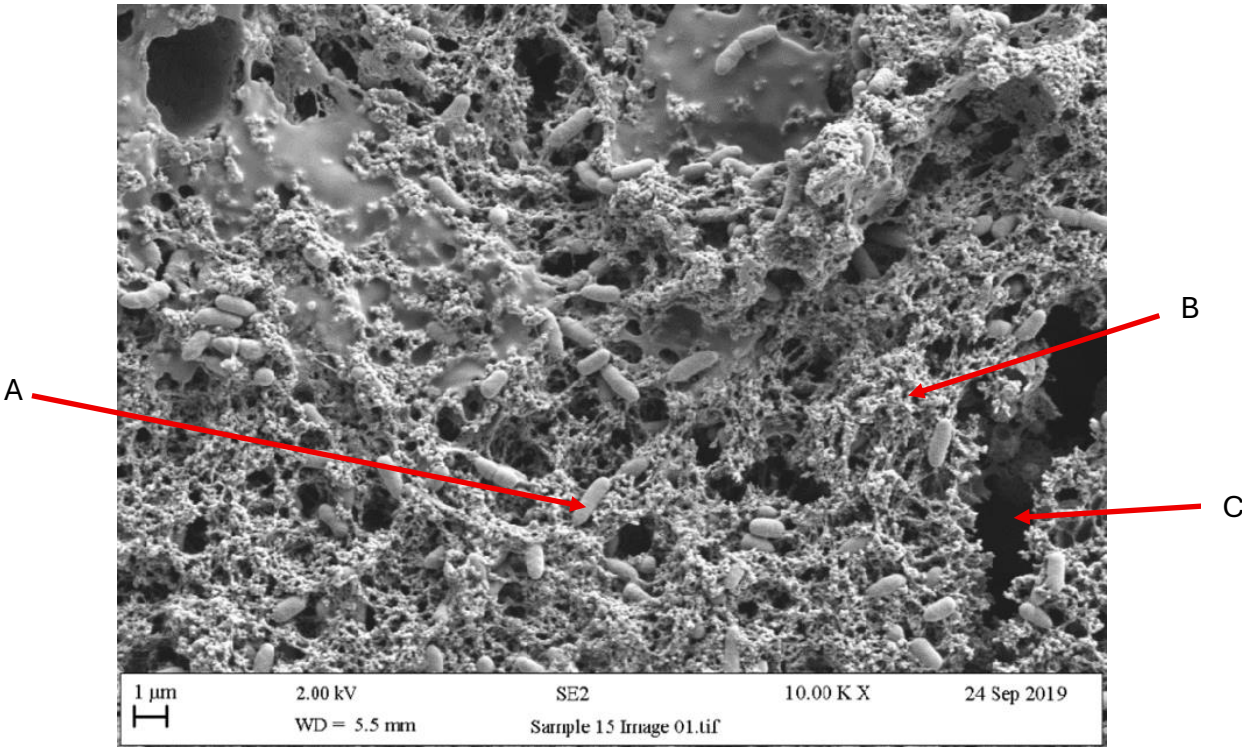

Figure 1.2. Scanning electron micrograph (SEM) of stainless steel with a mature bacterial biofilm. (A) Loose, rod-shaped bacterial cells. These represent planktonic bacteria that have not yet been fully encased in the protective EPS matrix. (B) A dense network of EPS. (C) The underlying stainless steel substrate, visible in areas where the biofilm is less dense.[8]

The maturation of a biofilm is an intricate, multi-stage process that typically proceeds through five discrete steps:

1) Reversible Attachment: Initial contact of free-floating (planktonic) bacteria to a surface through a combination of physical and chemical forces, including van der Waals and electrostatic attraction.

2) Irreversible Attachment: Bacteria attach to the surfaces using the appendages (e.g., fimbriae, pili, and flagella) which reinforce the bonds. This is where bacteria start to secrete EPS, forming a monolayer of protection.

3) Microcolony Development: Where the biofilm starts to form through multiplication and division, with EPS production increasing.

4) Maturation: Formation of the characteristic “mushroom” structure.

5) Dispersal: The biofilm releases bacteria to disperse and colonize new surfaces.[17]

Hence any successful outcome must not only kill isolated bacteria but also inhibit biofilm formation for a lasting effect. There are two common approaches using surface coatings as a medium to hinder microbial adhesion: an antimicrobial coating and an antifouling coating. Antimicrobial coatings work by actively killing or preventing the growth of microbes that are in contact with the surface. In contrast, antifouling proceeds by repelling microorganisms and

prevent them from attaching to the surface, initially using non-cytoxic surface characteristics.[18] Therefore, an integrated approach would be the most effective.

1.1.4 Cicada (Psaltoda claripennis)

Around 15 years ago, it became apparent to Australian researchers that cicada wings possessed the natural ability to kill Gram-negative *Pseudomonas aeruginosa* bacteria cells, which are known to be antibiotic resistant.[19] However, the mechanism remained unknown. Through electron microscopy it was found that the surface of cicada wings is comprised of arrays of needle-like nanopillars (see Figure 1.3) that have the capacity to puncture cellular membranes of bacteria that attempt to adhere to the wing surface. This solely physical mechanism disintegrates bacteria with widths around 1 μm, of similar size to the nanopillars, within approximately 3 minutes.[19] Additionally, while it is known that the cicada's superhydrophobic surface bestows its self-cleaning property, the suspected link between this self-cleaning ability and antifouling remains insufficiently explored.[20] The physicochemical influence of the cicada wing surface was evaluated by coating it with a gold film to isolate the role of surface nanopillars in its antimicrobial capabilities. Results revealed that its mechanical abilities remained unchanged despite the alteration of surface chemistry.[21] Hence why, Cicada wings therefore became the biological inspiration to achieving antimicrobial surfaces based on a purely physical mechanism.

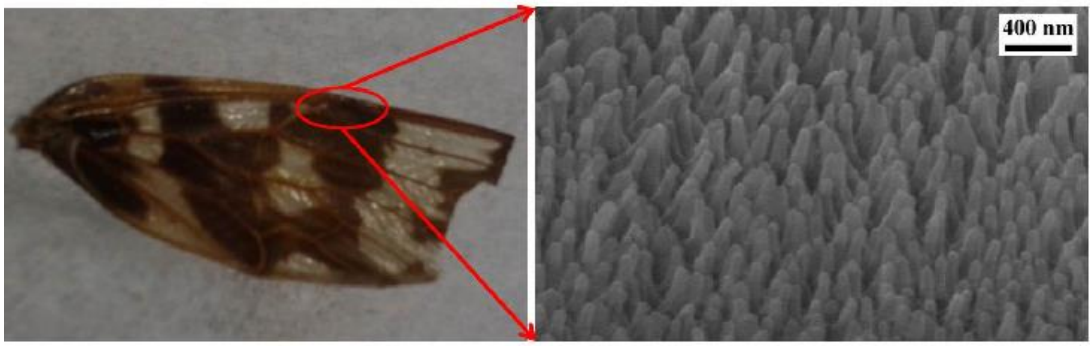

Figure 1.3. Cicada wings shown with nanopillars on their surface using SEM.[22]

1.2 Bacterial Cell Death

1.2.1. Physical Mechanism of Cell Lysis

Mechanical cell lysis is a method of cell death where the outer cell membrane is punctured using purely shear force, however, full understanding of the contact-induced mechanism remains unclear. Lysis is a direct mechanical rupture caused by surface topography stretching the bacterial cell membrane rather than the other common chemical (e.g. surfactants and detergents) or enzymatic methods (e.g. lysosomes).[22] This is important because this mechanical cell death bypasses biochemical resistance mechanisms.

This interaction is defined by a physical rupture of the cellular membranes at the interface with the nanopillars with the mechanism known as the 'bed of nails' effect. There is a physical threshold at which the cell membrane can no longer withstand the stress and strain and surpasses its survivable limit. This limit is consistent in all membranes at occurs at a critical compressive stress of 12.4 ± 0.6 kPa.[23]

While previous models concluded that bacterial membranes stretch between structures, a recent computational study by Velic *et al*. [24] elucidated a mechanism in which bactericidal rupture is driven by formation of a critical site at the pillar apex. This generates substantial in-plane strains that exceed the membrane's rupture limit, allowing for penetration and lysis of the cell. The resulting effect is that because of the cell rupture, the subcellular components such as DNA, RNA and proteins are released, effectively killing the cell. While these hypotheses receive experimental validation, the resulting conclusions fail to definitively explain the bacterial cell killing mechanism on nanostructures, with some conclusions alluding to a multi-faceted mechanism.

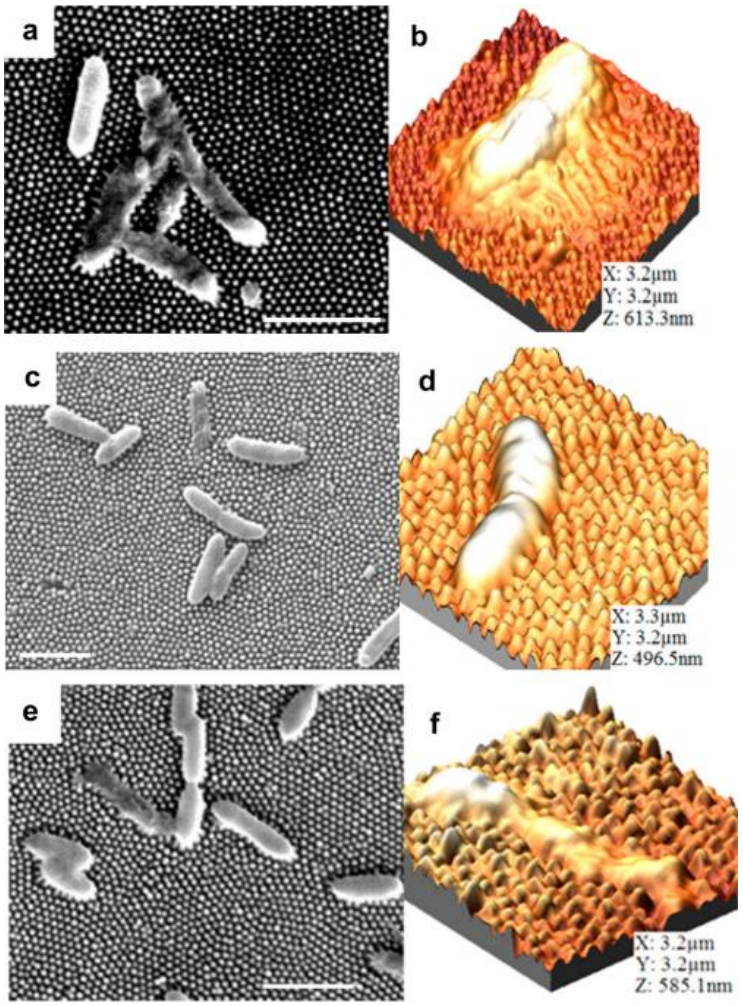

Figure 1.4. SEM and AFM images of fixed bacterial cells onto the wings of three cicada species: (a, b) M. intermedia *, (c, d)* C. aguila*, and (e, f)* A. spectabile*. Scales bars on SEM images (a, c, e) are 2 µm in length; All AFM images (b, d, f) are 3.2 x 3.2 µm.*[25]

1.2.2 Modelling Cell Death

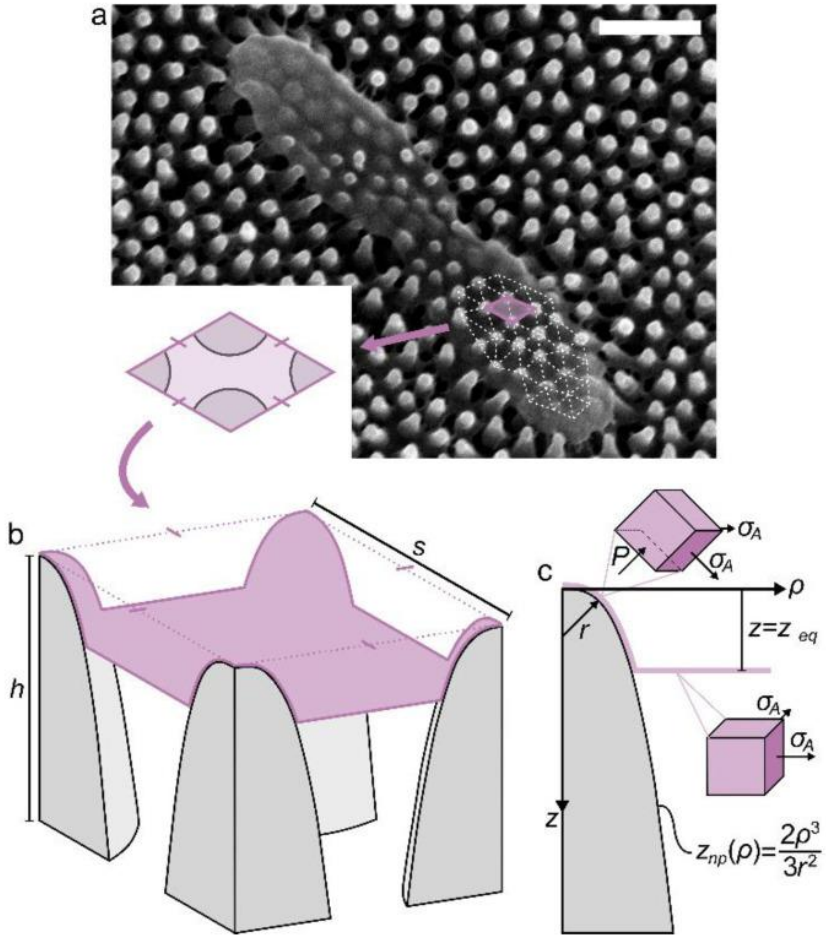

Figure 1.5. Model of the interaction between bacteria and a nanostructured surface. (a) Micrograph of bacteria on a Cicada wing, illustrating the entrapment of the bacterial cell envelope over the array of nanopillars. (b) Isolated area of four nanopillars with spacing (s) and height (h). (c) cross-sectional profile of a single nanopillar with an envelope attached. Nanopillars are modelled by $z_{np}(\rho)=2\rho^3/3r^2$*, where r is the quasi-tip radius. The bacterial envelope is adhered to the nanopillars at equilibrium sinking depth* z_{eq}*. This determines the resulting in-plane biaxial tensile stress (*σ_A*) and out-of-plane compressive contact pressure (P).* [24]

Velic *et al.* [24] also proposed a mathematical model describing cell death on nanopillars as shown in Figure 1.5. To allow for computational modelling, the nanopillars are assumed to be rigid. This assumption is corroborated by the elastic modulus of the nanostructured material typically being larger than the bacterial envelope. Ultimately, cell death is predicted when σ_A and P exceed the membrane's mechanical rupture threshold.

1.2.3 Antimicrobial Material Testing

Recently, adenine triphosphate (ATP) bioluminescence assays have been implemented which have the advantage of a rapid response time (within hours) and simplicity. This assay leverages on the fact that all metabolically active cells have ATP present, hence an enzyme is employed for any ATP-containing cells to bioluminesce. This works by using the enzyme luciferase which is oxidised to oxyluciferin when in the presence of ATP. Oxyluciferin produces light, so a luminometer is employed to measure the luminescence in relative light units (RLU), which is directly proportional to the amount of ATP in the cell. However, there are many limitations using this method. One is that it is non-specific, meaning there is no differentiation between live or dead bacteria, fungi or viruses. Additionally, since it detects ATP from *all* metabolically active cells, including food residue and organic soil, which can subsequently show false positive results for microbially clean surfaces.[26]

Another method utilises a nucleic acid live/dead bacterial viability stain, commonly the BacLight™ kit (see Figure 1.6), where bacteria can be visualised using a fluorescence microscope. This kit utilises a dual dye-staining system: STYO 9 and propidium iodide (PI). This works by assessing the resulting colour of the cells once the dye has penetrated the bacterial membrane. STYO 9 penetrates all cells and dyes them green. In contrast, PI can only penetrate damaged cell membranes and stains them red. From this, the relative number of live/dead cells can be counted to determine the material's antimicrobial success. This is therefore preferred over ATP assays as single cell visualisation can be done, so live bacteria and ATP from non-microbial cells can be differentiated.[27]

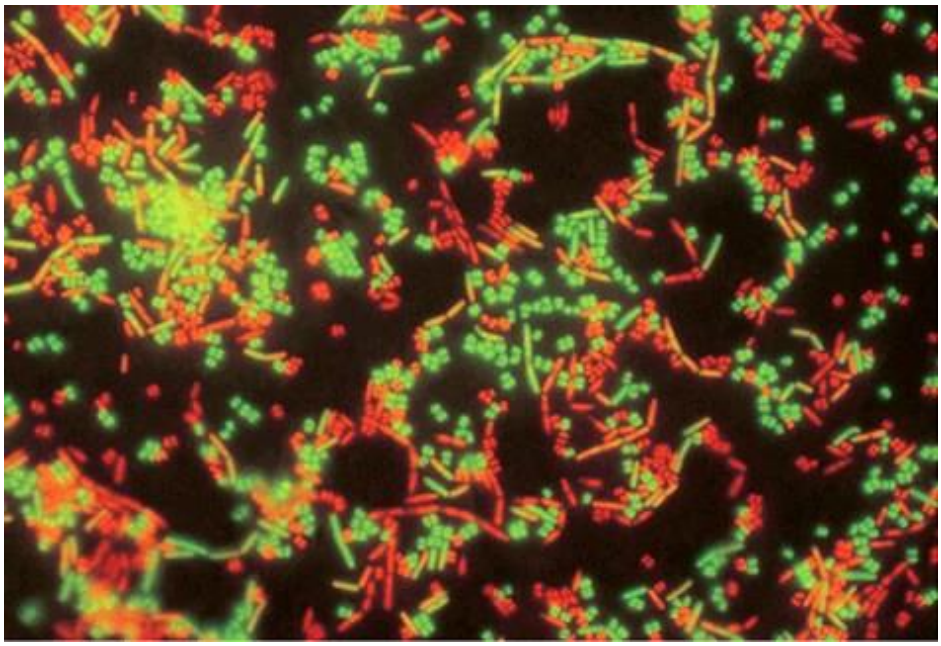

Figure 1.6. Micrococcus luteus *and* Bacillus cereus *stained with the BacLight Bacterial Viability Kit showing some living bacteria (green) and dead/dying ones (red).*[28]

1.3 Antimicrobial Surfaces

A diverse range of metals, encompassing both noble and transition elements, have been extensively researched for their inherent antimicrobial properties. The prevalence of literature focusing on these specific metallic coatings is summarized in Figure 1.7.

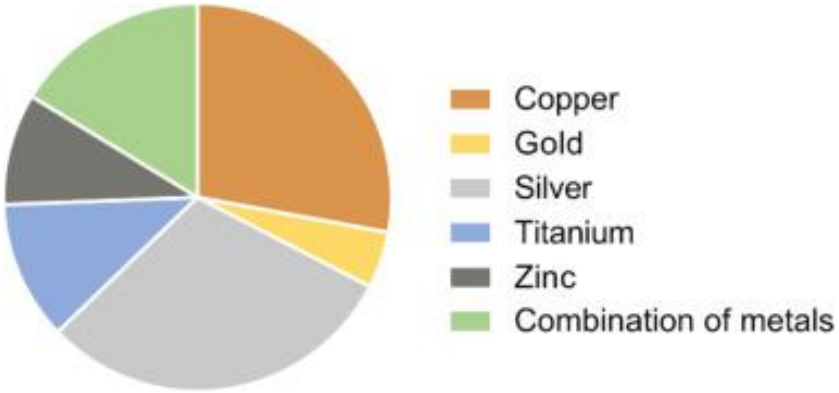

Figure 1.7. Percentage based graphical distribution of reviewed literature focusing on metal-based antimicrobial coatings. Each category represents a variety of chemical species, including pure elemental metals, stable metallic compounds, and reactive metal ions.[29]

1.3.1 Copper

Copper is an essential trace element for living organisms and has been used as an antimicrobial agent due to its potent antimicrobial properties for millennia, as recorded by ancient Egyptian artefacts.[30] As antibiotics became more prevalent in the 1930s, copper's use began to diminish. Copper surfaces have demonstrated their inherent antimicrobial properties, shown by eradicating bacteria and viruses where copper ions (Cu^{+} and Cu^{2+}) destabilise the microbial cell envelope and disrupt essential cellular processes.[31] However, the full mechanism is not yet fully understood. Clinical research has displayed these properties in microbes such as Methicillin-Resistant *Staphylococcus aureus* (MRSA), Vancomycin-Resistant Enterococci (VRE), *Escherichia coli (E. coli)*, and Norovirus.[32–34]

1.3.2 Silver and Silver Nanoparticles

Similarly to copper, silver was used as an antimicrobial agent in ancient civilizations and is still used today. Silver's antimicrobial properties are predominately exhibited in nanoparticle form where the physiochemical properties are different to those in the bulk due to the increase in surface area-to-volume ratio and reactivity. Silver nanoparticles leverage the same ion-release process seen in copper where cytotoxic effects are felt on bacterial cells through the sustained release of silver ions. Other mechanisms include membrane damage or intracellular DNA disruption.[35] However, as with copper, the exact mechanism of their antimicrobial properties is not fully understood.

1.3.3 Zinc

Zinc is commonly used for its antimicrobial activity in the form of zinc oxide nanoparticles (ZnONPs). ZnONPs allow for reactive oxygen species (ROS) generation to take place, where the ROS products are very toxic to microbial cells. Another common mechanism is Zn^{2+} ion release which damages the cell membrane and interferes in metabolic processes. Use of Zinc has already been extended to healthcare settings through its use in implants, antibiotic drugs and medical devices.[36]

1.3.4 Titanium

Titanium's optimum efficacy as an antimicrobial surface is in its metal oxide form (TiO_2). When exposed to UV light TiO_2 generates ROS that damage the bacterial cell wall.[37] While its biocompatibility, corrosion resistance and chemical inertness make it a preferred material for medical implants, implant-associated infections remain a prevalent complication. These infections are again attributed to bacterial colonisation.[38]

1.3.5 Polyethylene Glycol Based Coatings

Previous studies have demonstrated the passive antifouling properties of polyethylene glycol (PEG) coated surfaces against Gram-negative and Gram-positive bacteria, as well as fungi. PEG is a hydrophilic polymer that proceeds by creating a dense, hydrated layer on the surface that acts through a combination of a steric barrier and excluded volume effects. These make it physically difficult for bacteria to adhere to the surface preventing biofilm formation. For maximum repulsion, a PEG polymer brush with high grafting density is the most effective method to eliminate potential adhesion sites. Initial results show that PEG has an adhesion reduction of 90-99% for *S. aureus* and *P. aeruginosa.* However, its long-term performance is limited, as it undergoes oxidative degradation, making it unsuitable for everyday use.[39]

1.3.6 Metal-Organic Frameworks

Recently, researchers from Chalmers University of Technology, Sweden won the 2025 Nobel Prize in Chemistry for engineering microscopic metal-organic framework (MOF) spikes to mechanically kill bacteria.[40] The material is a MOF-on-MOF hybrid called MoU, using a zirconium-based UiO-66 core and iron-based MIL-88B satellite that grows into nanospikes. Their results demonstrated an 83% killing efficacy against *E. coli* (Gram-negative bacteria). However, they encountered a problem that would affect the long-term success of the surface. They found that after 72 hours, the efficacy drops from 83% to 51%, likely attributed to the accumulation of dead bacterial, effectively masking the spikes.[41] Hence, this presents the need to fabricate a surface that exhibits self-cleaning properties for long-term efficacy.

1.3.7 Black Silicon

Recent work in this field has been focused on developing surfaces that replicate the antimicrobial mechanisms naturally found in nature that are inexpensive, and which also have the potential to be scaled up and incorporated into everyday life. Black silicon (bSi) is a synthetic semiconducting nanomaterial that is fabricated through lithography and reactive-ion etching (RIE) of regular silicon.[42] This yields micro- and nanoscale protrusions on the Si

surface of varying length, areal density and sharpness, where these parameters can be precisely altered to enhance its efficacy against rupturing bacterial cell membranes.[43] Other promising applications of bSi include solar cells, photodetectors and drug delivery.[44–46] The nomenclature of the material stems from its optical properties; narrow interstitial gaps between the nanopillars reduce light reflection, resulting in its ability to trap >99% of visible and infrared wavelength light across the spectrum. The result of this is its appearance is very black.[47]

Despite its antimicrobial capacity, the primary problem with bSi surfaces remains the fragility of the nanopillars, which are prone to structural fracture under minimal external force.[48] Thus, for its bactericidal activity to be utilised in real life, bSi needles need to be more mechanically stable while preserving their antibacterial effects. One method that had shown promising results is deposition of a thin film diamond layer on a bSi surface to create black diamond (bD), which can be evaluated against a flat diamond (Flat-D) control layer (see Figure 1.8).[49]

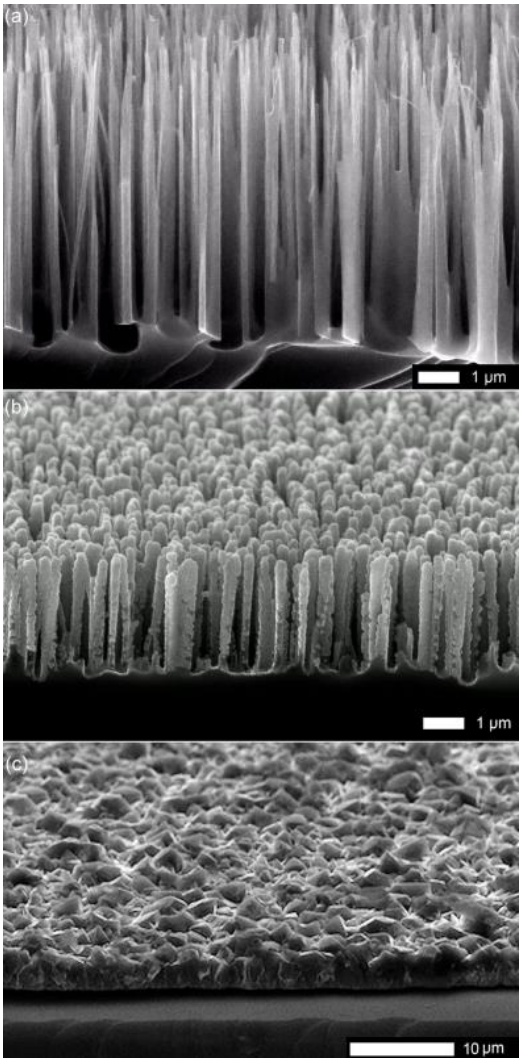

Figure 1.8. SEM images of a) bSi wafer cross section, b) bD wafer cross section, and c) 'flat' diamond control layer (i.e., a continuous nanostructure-free polycrystalline diamond film on a Si substrate).[50]

1.4 Polymer Replication

Antimicrobial polymers show promise as an alternative to bSi or bD due to their cost-effectiveness, tuneable structures, and chemical inertness.[51] To transfer the technology developed in bD to cheaper polymers, various lithography techniques can be used for their fabrication.

1.4.1 Nanoimprint Lithography

Nanoimprint lithography (NIL) is a mechanical fabrication technique with low cost and low power usage, allowing for mass fabrication.[52] In this technique, a substrate is coated with a thin layer known as a resist. This resist is a polymer, and the master mould (in our case the bD surface with the desired nanostructures) is pressed into the resist to transfer the pattern. As the mould is pressed down into a deformable material, the resist is then hardened either via heat (thermal-NIL) or UV light (UV-NIL). The mould is then lifted, leaving behind a perfect negative reproduction, of sub-100 nm structures (holes), on the substrate.[53]

Thermal NIL uses a thermoplastic polymer film that is coated onto the substrate (see Figure 1.9(a)). This film is then heated above its glass transition temperature (T_g), the point at which it becomes soft and malleable. This is when the template is pressed into film under high pressure and the fluid material occupies the mould. Finally, after cooling below T_g, the mould is removed, leaving an inverse replica of the template pattern in the polymer.[54]

UV-NIL is distinguished from normal NIL by two primary advantages: the ability to operate at low temperatures and the requirement for low pressure instead of high pressure (see Figure 1.9(b)). For this to work, the polymer solution needs to have low viscosity and be UV-curable. The polymer is dispensed via spin-coating onto the substrate. The template, which must be UV transparent, allow the polymer to photoisomerise when it is exposed to UV light. Essentially, this is a photochemical reaction that changes the polymer from liquid to solid. Again, an inverse 'negative' pattern of the template is left behind. UV-NIL is the preferred method as it is generally faster than thermal-NIL as it avoids lengthy heating and cooling cycles and can work under room temperature and low pressure.[55]

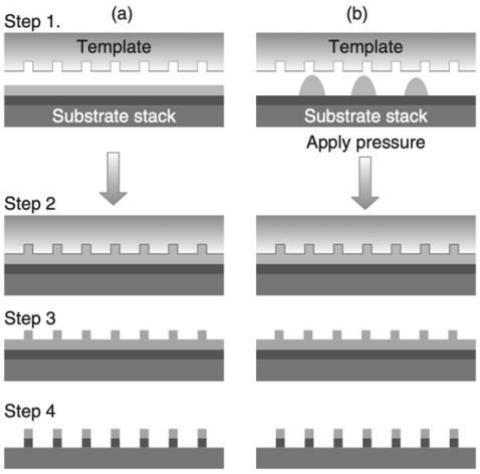

Figure 1.9. Schematic diagram showing the process of (a) Thermal-NIL (b) UV-NIL.[56]

UV-NIL is an alternative to conventional photolithography where a light source is directed toward a photosensitive polymer, with aims to pattern it through a photoresist mask. Whilst this method is traditionally used it has some limitations; one being the wavelength of light required and another the expensive lenses and complex light sources that are needed. Hence, NIL offers an alternative technique with numerous advantages through use of a high-quality mould and precision press.[57]

1.4.2 Soft Lithography

In this process, a master template (in our case the Si surface patterned with nanoholes) is coated with a 'soft' polymer that is dispensed manually or via a spin coater. These polymers are referred to as elastomers which are characterised by being physically flexible and their ability to be stretched or compressed and subsequently return to their original shape. Following deposition, the polymer is then hardened with UV light. The polymer is then lifted, leaving behind a negative reproduction, of sub-100 nm structures, on the polymers surface. Figure 1.10 illustrates the photochemical reaction that essentially transforms the polymer from a liquid state to a solid state.

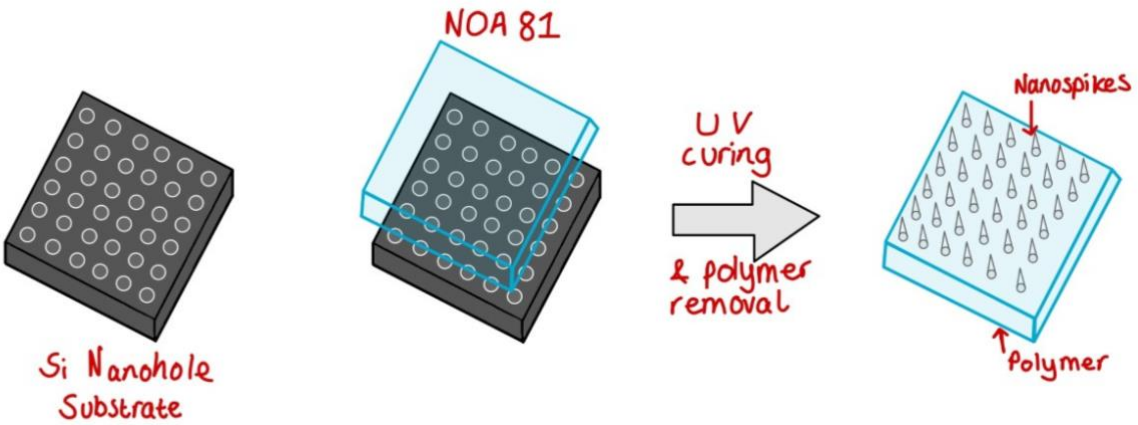

Figure 1.10. Schematic diagram showing the process of soft lithography.

Soft lithography is an alternative to conventional photolithography where a light source is directed toward a photosensitive polymer, with aims to pattern it through a photoresist mask. Whilst this method is traditionally used it has some limitations; one being the wavelength of light required and another the expensive lenses and complex light sources that are needed. Furthermore, soft lithography template substrates are reusable, in contrast to the limited durability of the master template in photolithography. Hence, soft lithography offers an alternative technique with numerous advantages through use of a high-quality polymer.

1.4.3 Candidate Polymers: PDMS and NOA-81

It is crucial to find a polymer that is compatible with soft lithography while also possessing the necessary mechanical properties for it to be effective as an antimicrobial surface. Poly

(dimethyl siloxane) (PDMS) is a commonly used soft polymer owing to its transparency, biocompatibility, and ease of manufacturing,[58] and is an obvious candidate for soft lithography. Unfortunately, experiments have revealed numerous limitations as to why PDMS is fundamentally unsuitable for soft lithography. Firstly, Berthier *et al*. determined that PDMS lacks the scalability required for mass production.[59] Additionally, it has a Young's Modulus of around ~1.5 MPa, dependent on its mixing ratio, which effectively leads to deformation of the nanopillars under mechanical stress.[60] Previous research confirms this, where demoulding of PDMS using soft lithography results in structural distortion when replicating. In particular, the height of the nanostructures increased by 10-60% in comparison to the master mould.[61]

Researchers tried to overcome the inherent drawbacks of PDMS by considering alternative materials, such as the optical glue Norland Optical Adhesive (NOA-81). The material cures via a UV-initiated thiol-ene click reaction between a mercapto ester (Figure 1.11(a)) and Triallyl isocyanurate, the monomer (Figure 1.11(b)). This material is determined to be a biocompatible substitute for PDMS in microfluidics, microchannel fabrication, and cell culture devices.[62,63]

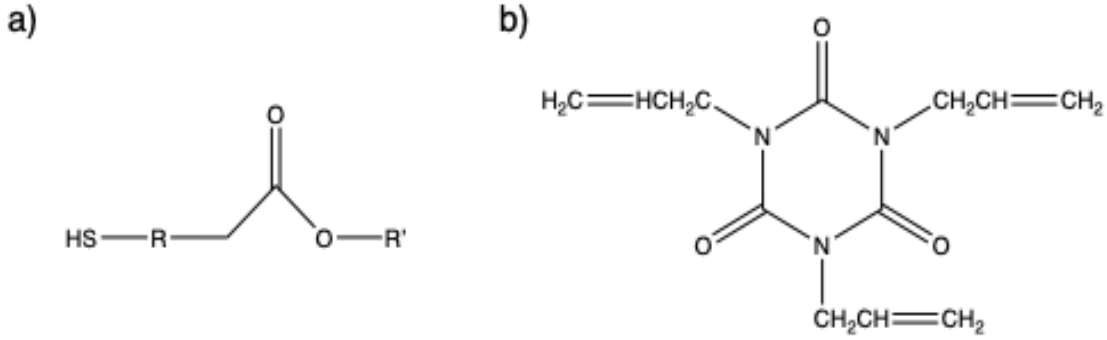

Figure 1.11. (a) General structure of mercapto ester, (b) Triallyl isocyanurate.

It has a high Young's modulus of 1 GPa which enables a high-aspect-ratio topography without compromising its rigidity. NOA-81 is also compatible with UV-NIL, therefore making it suitable for rapid processing and high-throughput.[64] However, challenges using NOA-81 for NIL include controlling the film thickness and ensuring it is uniform over the substrate.

1.4.4 Challenges

A major challenge is determining the perfect parameters, specifically the distance, height and density of the nanostructures. If the gap between protrusions is too small, bacteria are more likely to survive as mechanical stress is distributed across the membrane (the 'bed-of-nails' effect). Conversely, if the gap is too big, bacteria can slip through and bind to the surface or orientate themselves to preferentially minimise contact stress. Fine tuning this geometry will maximise the antimicrobial effects. The minimum optimal spacing between nanopillars has been found to be between 130 nm and 380 nm with an average pillar density of ~ 40 pillars μm^{-2}.[65,66] Additionally, the optimal length of nanostructures is found to be between 120 nm and 220 nm.[67] This could be because if they are any longer the nanostructures are susceptible to

bending, and will therefore have no further impact on killing bacteria. If they are shorter, they cannot penetrate the cell membrane. Discrepancies remain among previous literature regarding optimal parameters, which will be further explored in future research.

Another particular challenge in using polymers is determining the hardness-to-wetness ratio. The polymer must be sufficiently fluid (low viscosity) to mould to the master template yet also hard enough when cured that it can easily be removed without damaging the final nanostructured polymer surface. This is particularly difficult since polymers are inherently viscous. Additionally, the interaction between bacterial attachment and the different hydrophobic surfaces is yet to be determined, as explained before. Finally, air pockets commonly form within the template, distorting the nanostructures. To mitigate this vacuum is used prior to UV curing. This is implemented to evacuate trapped air from the template-polymer interface, in turn preventing the formation of bubbles that would otherwise compromise the structural integrity and geometric precision of the resulting nanostructures.

1.5 Diamond Chemical Vapour Deposition

1.5.1 Properties of Diamond

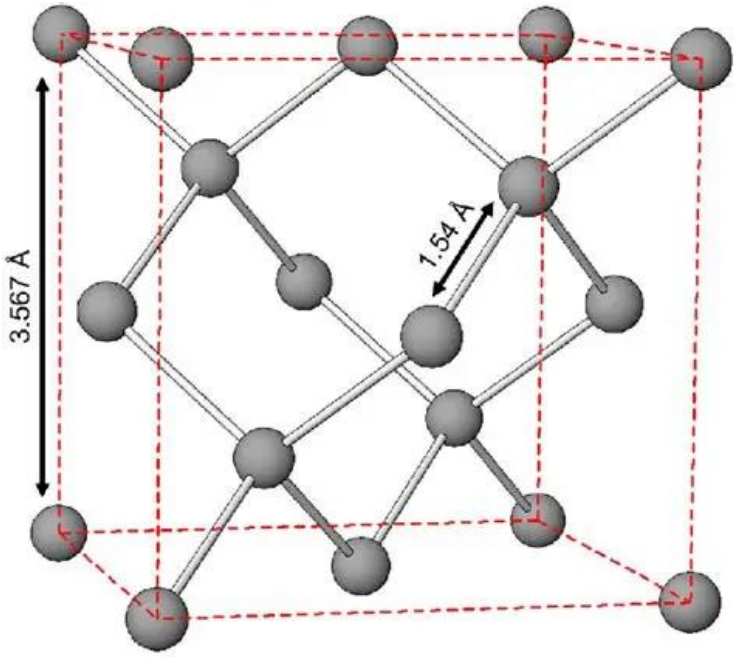

Figure 1.12. Ball and stick model of tetrahedral diamond lattice.[68]

Diamond's origins are believed to have been in India, with the earliest record dating back to the 4th century.[69] Diamonds have always been appreciated for their beauty and rarity; nevertheless, it is only within the last century that their extraordinary physical and electrochemical properties have been recognised. Geometrically, its structure is formed from sp^3 hybridised carbon, which gives its tetrahedral geometry arranged in a cubic-face centred lattice (Figure 1.12).[70] There are numerous superlative physical properties that make it a

desirable material such as its unmatched mechanical strength, high thermal conductivity and favourable optical dispersion (Table 1). In this research, its mechanical strength is of greatest importance making it an ideal candidate to improve the robustness of black Si needles (see section 1.3.7). Given these properties, synthetic diamond has numerous applications including medical implants, electrochemistry, solar energy generation and optical lenses.[71,72,73,74]

Property	**Value**
Chemical reactivity	Inert
Hardness / (kg mm^{-2})	10,000
Strength, tensile / GPa	>1.2
Strength, compressive / GPa	>110
Density / (g cm^{-3})	3.52
Young's Modulus / GPa	1.22
Thermal Conductivity / (W cm K)	20.0
Optical index of refraction (at 591 nm) / dimensionless	2.41
Optical transmissivity (from nm to far IR) / dimensionless	225

Table 1: Properties of Diamond.[75]

1.5.2 CVD Diamond

Chemical Vapour Deposition (CVD) is used to synthesise high-quality single crystals, microcrystalline, and nanocrystalline diamonds.[76] The deposition of diamond proceeds via a surface-gas phase mechanism. For diamond growth at low pressures, an activation source, such as plasma or heat, fragments molecular hydrogen (H_2) into highly reactive atomic hydrogen (H). These hydrogen radicals then react with methane (CH_4) in the gas phase to generate methyl radicals (CH_3), which serve as the primary precursor for diamond deposition. The atomic hydrogens then diffuse and react with the substrate, abstracting the terminal hydrogen atoms to create vacant radical sites. While most of these vacancies are re-occupied by hydrogen which preserves diamond formation, CH_3 occasionally reacts here to facilitate growth of the diamond lattice. The higher concentration of H_2 works here to preferentially etch sp^2 carbon impurities, ensuring there are no non-diamond carbon forms on the surface (e.g. graphite).[77] This mechanism is shown in Figure 1.13. While the fundamental chemical process remains the same, various methods exist in order to provide the energy required for gas activation, including Microwave Plasma CVD (MPCVD) and plasma-enhanced CVD (PECVD).[78]

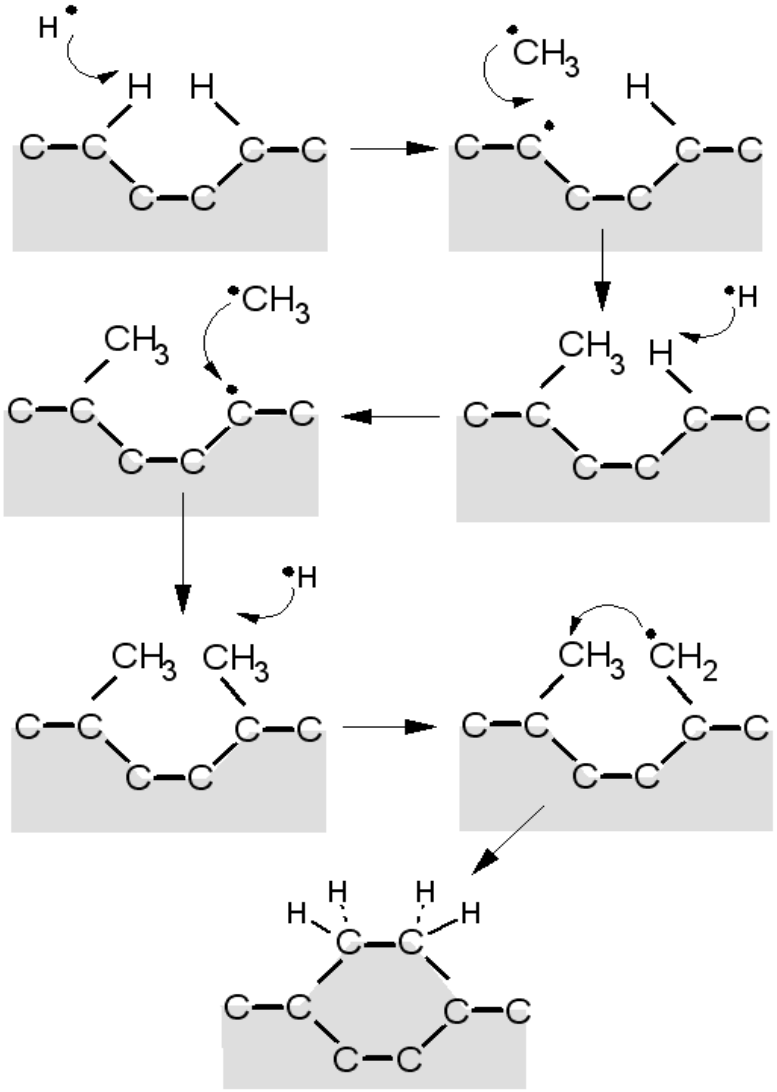

Figure 1.13. Simplified reaction scheme of the Standard Growth Model for CVD diamond.[77]

1.5.3 Hot Filament CVD

One method of CVD is hot-filament CVD (HFCVD), which originated at the NIRIM by Matsumoto et al. in 1982.[79] It is distinguished compared to other CVD methods through its technical simplicity and capacity for large-area deposition.[80] Here, within the vacuum chamber, thermal energy from heated filaments— commonly Tungsten (W) or Tantalum (Ta) due to their high melting points— is used to fragment H_2 (see Figure 1.14). The temperature of the filaments here are 2000-3000 °C. The radicals then follow the growth mechanism described in section 1.5.2. The end product for growth on a black silicon substrate is referred to as black diamond. The process for creating non-doped diamond films starts by seeding a bSi surface with nanodiamond. Seeding is essential to provide nucleation sites for the reactions to take place, since diamond does not spontaneously deposit on non-diamond substrates.

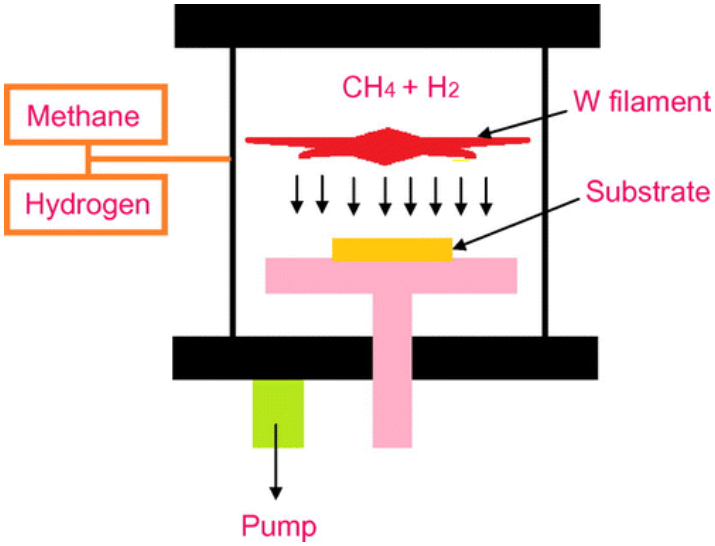

Figure 1.14. Schematic diagram of a hot filament CVD reactor.[81]

1.5.4 Diamond Surface Termination

While the bactericidal mechanism is physical, the chemical properties, and hence how the nanostructures interact with bacteria, can be altered by changing the surface termination of the bD surface. At the end of CVD growth, the sample is H-terminated. To transition to a hydrophilic state, oxygen termination is utilised via UV/Ozone (UVO), resulting in water contact angles (WCA) < 90°. Conversely, fluorine termination achieved using SF_6 plasma in a DC reactor, creates a super-hydrophobic surface with a WCA > 150°, as demonstrated by the water-droplet test in Figure 1.15.[82] Previous work determined that both the fluorine-terminated and hydrogen-terminated bD surfaces showed the strongest antimicrobial activity.[83] In contrast, other literature suggest that hydrophilic surfaces are better at repelling bacteria and minimising biofilm formation.[84]

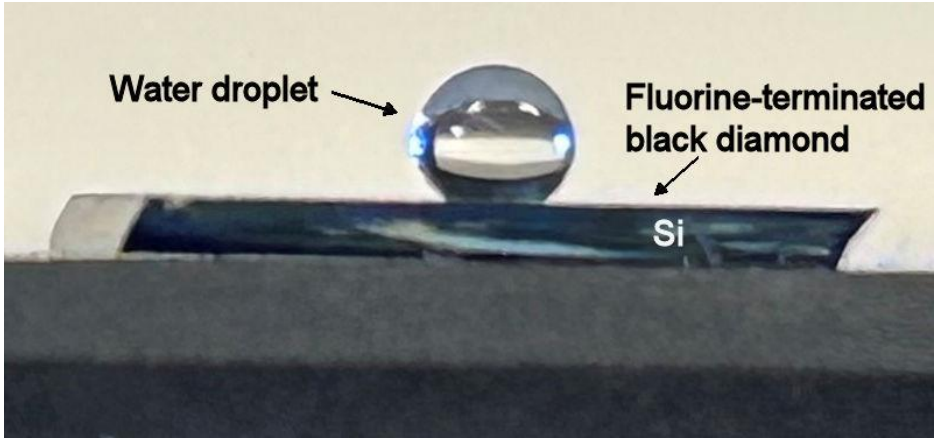

Figure 1.15. Water-droplet test on F-terminated black-diamond surface.[85]

As promising as the antimicrobial uses of diamond films are, there is the growing need for a material that can produce the same high-performance output at a lower cost and increased scalability.

1.6 Prior Work

Recently, with the rise in AMR, research efforts have pivoted towards mechanical strategies. Previous work has successfully fabricated nanostructures on silicon surfaces to kill bacteria. While this has proven to be successful against gram-negative bacteria, its fragility hinders it applications in the real world. To address this, the Diamond Group at Bristol improved this through the development of bD which solved the inherent fragility of silicon nanostructures, however the high cost and scalability issues remain a significant hurdle.

To address this, recent research within the group has pivoted toward polymer-based surfaces to ultimately achieve the same result as bD. This project extends on polymer replication research previously done within the Diamond Group using PDMS. It was found that using NIL to create a negative copy of bD using PDMS was unsuccessful.[86] This initial research provided a pathway for this project, shifting the focus towards soft lithography with NOA-81.

1.7 Project Aims

This project seeks to advance the fabrication of cost-effective, mechanically robust antimicrobial surfaces by considering two distinct approaches: bD and polymer-based biomimetic surfaces. By leveraging their high-aspect-ratio topographies, this work overall aims to contribute to the transition from traditional chemical biocides toward physical-mechanical bactericidal mechanisms.

The first objective focused on fabricating high fidelity nanostructured and control substrates. This involved producing a range of samples- including flat silicon (control), bSi, bD, and Flat-D- to be sent to the University of Groningen in the Netherlands for comparative antimicrobial efficacy testing against *E.coli*.

The second objective sought to establish a novel polymer replication method via an experimental soft lithography technique. This involved the development and evaluation of a replication technique using NOA-81 to produce negative nanostructured replicas from silicon nanohole templates.

2. Methodology

2.1 Sample Preparation

2.1.1 Black Silicon

Twelve-inch bSi wafers were acquired from LAM Research Corporation (USA). Manufacturing of the nanoneedles on the surface was done via RIE with SF_6/O_2. The samples were mechanically fractured into 1 cm^2 sized squares using a diamond-tipped scribe and tweezers for use in the diamond chamber.

2.1.2 Silicon

The Oxford Lasers Alpha 532-XYZ-A-U micromachining system, shown in Figure 2.1, was used to cut the purchased Si (100) wafers into 1 cm^2 squares for Flat-D growth in the HF-CVD reactor. The adoption of smaller substrates for both Silicon and bSi wafers was required for antimicrobial testing purposes.

Figure 2.1. Image of Oxford Lasers System.

2.1.3 Seeding

To enable diamond growth on the non-diamond substrate, the bSi substrates were seeded using nanodiamond to provide a nucleation. A nanodiamond suspension was prepared by diluting 10 drops of detonation nanodiamond colloid solution (NanoAmando Colloid 3.3 ± 0.6 nm) in ~30 mL methanol. The solution was then sonicated for 3 hours using an ultrasonic probe at 40% power. Once sonicated, the bSi samples were submerged in the suspension for one hour in a

petri dish. The samples were then air-dried for 30 minutes before storage or growth. Seeding the samples with nanodiamond crystals enhanced the nucleation density, thereby accelerating the diamond growth rate.

The silicon wafers were seeded using manual abrasion. Nanodiamond powder (1-3 μm) was placed between two silicon wafers and mechanically abraded against one another for ~5 minutes to seed the surface.

2.1.4 Diamond Growth

Thin, poly-crystalline diamond layers were deposited onto the seeded substrates using HF-CVD, as illustrated in Figure 2.2. HF-CVD is the preferred method due to its low operating costs, scalability and ease of use. However, a major drawback in using this method is the short-term stability of the filaments and contamination of the resulting diamond film. As the filaments undergo corrosion and carbide formation, it culminates in inconsistent deposition.[87] For the purposes of this study and taking into consideration this is a university lab-based project, a high-purity surface isn't imperative.

Seeded bSi samples were placed below three filaments made of tungsten wire (Figure 2.3). The samples were then loaded into the reaction chamber which was subsequently evacuated to a base pressure of $< 10^{-2}$ Torr before initiating growth. Once vacuum was established the chamber was heated for 30 minutes. The chamber pressure was maintained at ~ 20 Torr with a current of 25 A applied to the fresh tungsten filaments. The temperature of the substrates was ~900 °C and the filaments at 2400 K Once conditions were stable, the process gases were injected for 30 minutes with the following parameters: CH_4 (1%) diluted in an excess of H_2 (flow rates of 2 sccm and 200 sccm respectively). All depositions were performed under the same parameters. CH_4 was then turned off and H_2 was left pumping for a minute longer at the end of each run for the resulting bD product to be H-terminated.

Control diamond film samples, deposited on flat Si wafers, followed identical growth conditions; however, the growth duration was increased to 6 hr to achieve a uniform film coating.

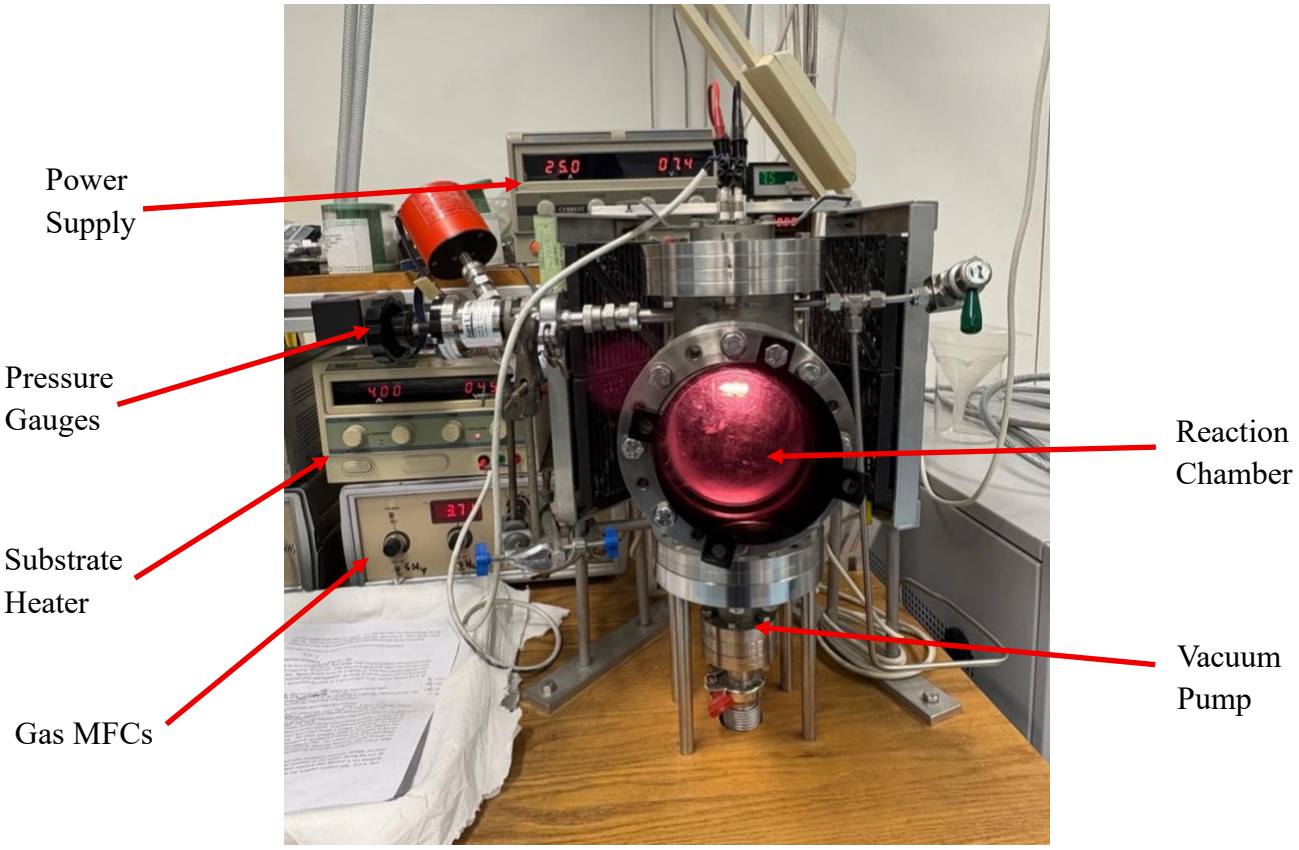

Figure 2.2. Annotated image of HF-CVD reactor.

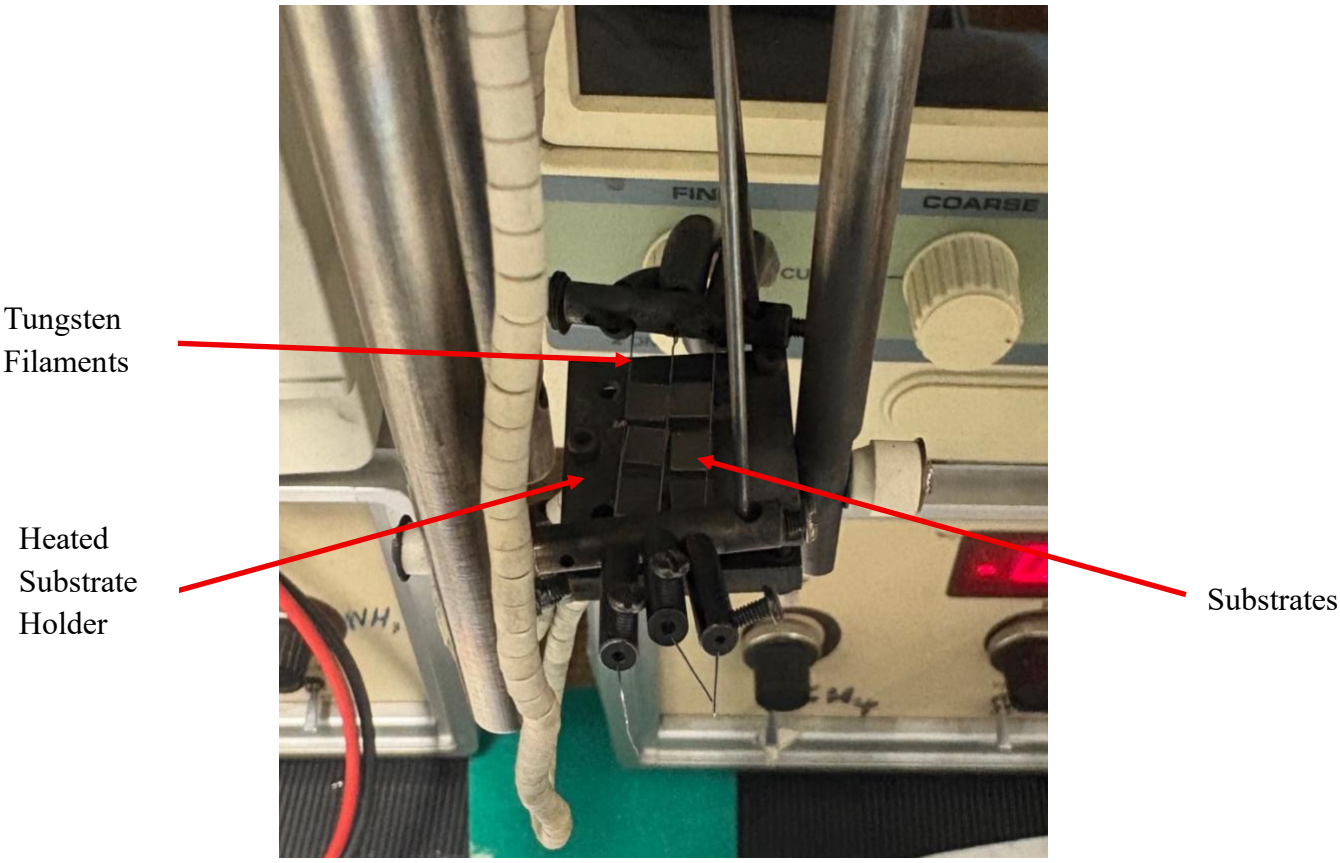

Figure 2.3. Annotated image of the substrate holder used in the HF-CVD reactor.

2.1.5 Termination

For fluorine termination, substrates were placed in a DC plasma reactor (Figure 2.4) to replace the C-H bonds with C-F bonds to increase the hydrophobicity of the surface drastically. Firstly, air was evacuated, and argon was injected for 10 minutes to remove any residue contaminants. The chamber was then pumped down to vacuum (< 10 mTorr) and SF_6 was injected until the pressure reached 1 Torr. A voltage was applied to the sample tray for ~10 seconds to create a plasma produced by SF_6 over the surface.

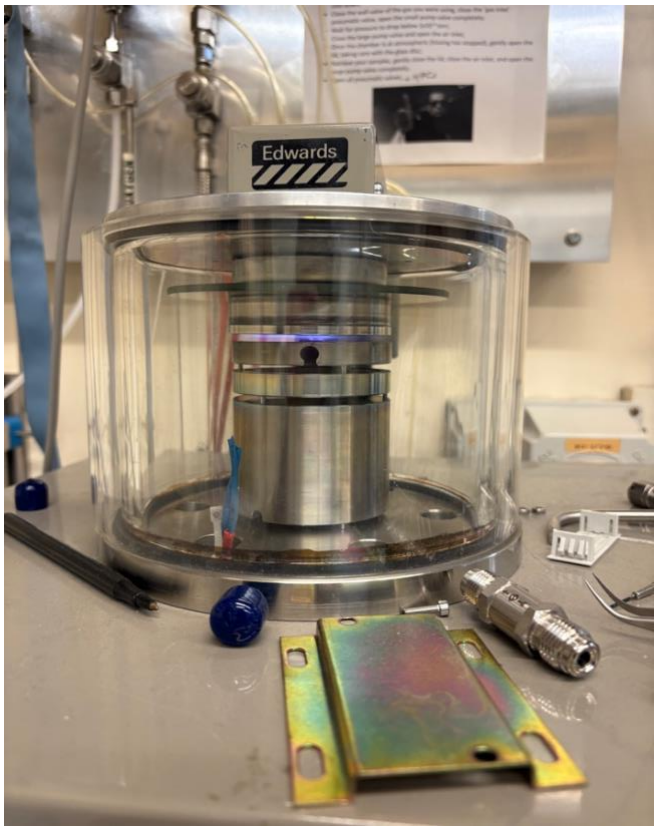

Figure 2.4. Image of DC plasma reactor.

For oxygen termination, samples were exposed to UVO treatment using a UVO-cleaner kit (Model 42, Jetlight Company Inc.) at the Bristol electrochemistry laboratory. The samples were exposed to UVO for 25 minutes.

2.2 Characterisation of Samples

2.2.1 Raman

Renishaw Ramascope 2000 Raman system was used to record Raman measurements of the fabricated diamond films (see Figure 2.5). A 514 nm Ar^+ green laser was utilised at a power of approximately 30mW. The chemical bonds within the substrate are probed and scatter light,

where the resulting wavelength shifts generates a structural fingerprint unique to the molecule. To calibrate the instrument, a high purity single crystal diamond was used. To maintain sample integrity and prevent thermal degradations of the surface, the laser power was optimized for each substrate. Additionally, the exposure times and acquisitions were refined to achieve high resolution spectra. For the bD samples, single acquisitions using a 1-second exposure time at 1% power was used. In contrast, the bSi samples requires 10 acquisitions with a 5-second exposure time at 33% power to compensate for the materials >99% absorption of light. The central wavenumber was set to 1332 cm^{-1}, allowing for definitive identification of the characteristic sp^3 crystalline diamond peak. For diamond films grown through HF-CVD, there are commonly additional signals within the spectrum correlating to graphitic grain boundaries, ultimately reducing the quality of diamond crystal growth.

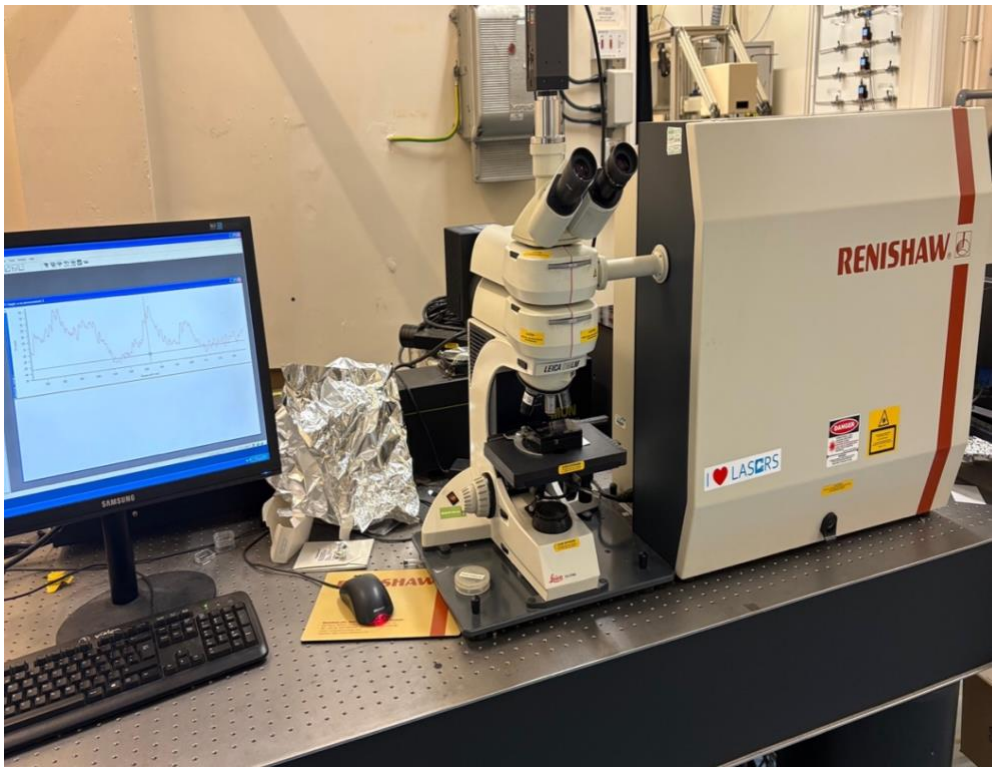

Figure 2.5. Image of Renishaw Ramascope 2000 Raman system.

2.2.2 Water Droplet Contact Angle

The surface hydrophobicity of the samples was evaluated via static WCA measurements using a Kruss Droplet Shape Analyser (see Figure 2.6). To determine the contact angles, a drop of deionised water with a volume of 1.5 microlitres was dispensed onto the sample via a nanodispenser tip. The droplet profile was captured via a side-facing camera within 1-2 seconds of the drop being placed on the surface.

Trimethylchlorosilane (TMCS) was used for silanisation of some Si, bD and Flat-D wafers in gas. The wafers were placed inside a Petri dish where a few droplets of TMCS were added

around the wafers. Next, The Petri dish was closed for 15 minutes after which it was opened and the TMCS was allowed to evaporate over 10 minutes prior to angle testing.

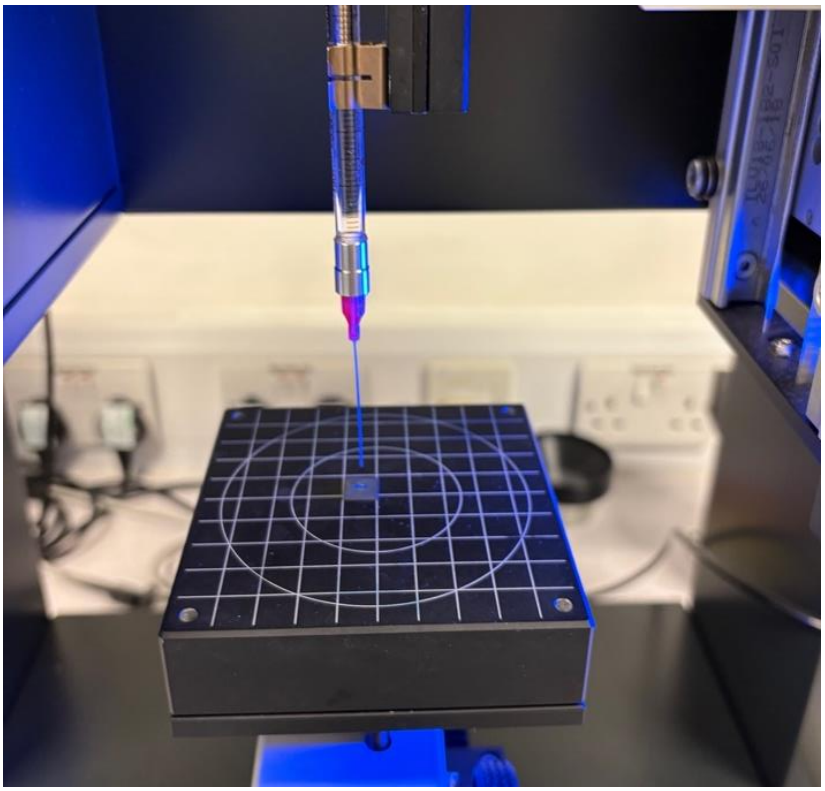

Figure 2.6. Image of Kruss Droplet Shape Analyser.

2.2.3 Scanning Electron Microscopy

The surface nanotopography of bSi and bD films was characterised using a JEOL IT300 SEM (see Figure 2.7). SEM works by projecting a focused stream of high-energy electrons and the electrons reflected off the sample produce a high-resolution image. Images were acquired from both top and cross-sectional views at various magnifications. For cross-sectional analysis, the Oxford Lasers system was used to cut samples in half, where the samples were mounted at angle of 70 degrees. All images were captured using an accelerating voltage of 15/20 kV and a working distance of 8-9 mm.

To mitigate charging effects and ensure high-resolution imaging, the non-conductive NOA-81 nanostructured substrates were mounted to the sample holder using conductive copper tape.

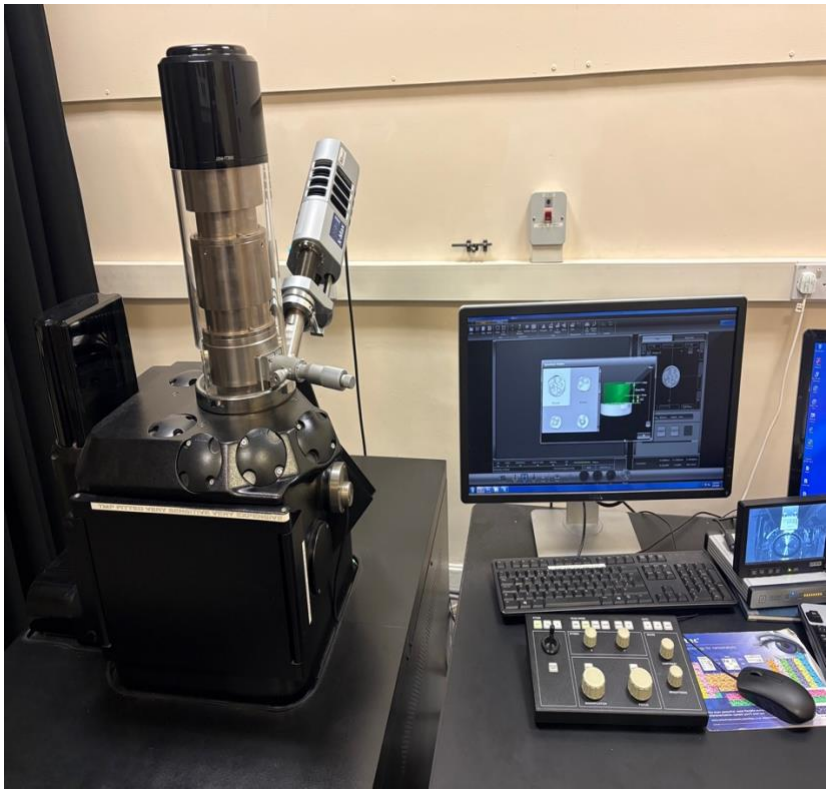

Figure 2.7. Image of JEOL IT300 SEM.

2.2.4 LEXT Laser Microscope

Figure 2.8. Image of Olympus LEXT OLS5100 microscope.[88]

3D surface topographies and 2D surface profiles were acquired using an Olympus LEXT OLS5100 3D laser confocal microscope (see Figure 2.8). The microscope utilized a 405 nm laser with observations conducted at various magnifications between 10x and 100x.

2.3 Polymer moulding

2.3.1 Silicon nanohole fabrication

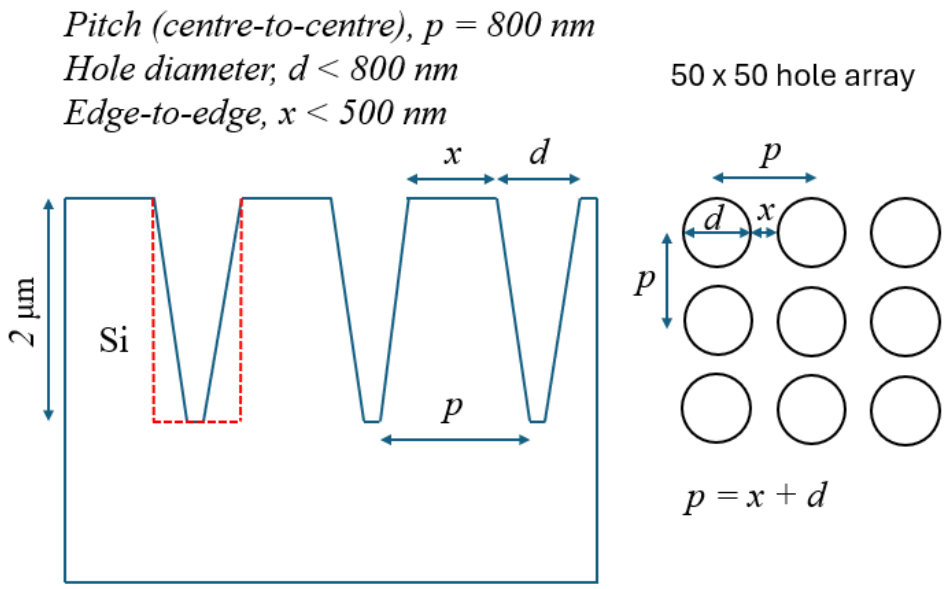

Figure 2.9. Diagram showing the parameters controlled for fabrication of the silicon nanohole substrate.

The synthesis of silicon nanohole surfaces was executed via electron beam lithography (EBL) in the physics clean room. Initially a deposition of a 250 nm SiO_2 film onto 10 mm x 10 mm silicon wafers using PECVD was carried out. This functioned as a hard mask for subsequent etching steps. A polymethyl methacrylate (PMMA) electron-sensitive resist was next spin-coated onto the SiO_2 substrate, followed by electron beam irradiation to transcribe the design (see Figure 2.9) programmed in the lithography software. Post-exposure, the resist was hardened to define the nanohole design. The pattern was transferred into the underlying SiO_2 layer via Inductively Coupled Plasma Reactive Ion Etching (ICP-RIE) using a CHF_3 (50 sccm) and Ar (5 sccm) at a pressure of 15 mTorr and 50 W RF power. Following mask etching, the remaining resist was removed using a resist remover. The exposed silicon was anisotropically etched through the SiO_2 hard mask via ICP-RIE, utilizing a gas mixture of SF_6 (15 sccm) and CHF_3 (40 sccm) at a pressure of 13 mTorr, an RF power of 10 W, and an ICP power of 700 W to reach a feature depth of ~2 µm. Subsequently, the SiO_2 hard mask was removed using hydrofluoric acid (HF) to expose the finalized nanohole substrate (see Figure 2.10).

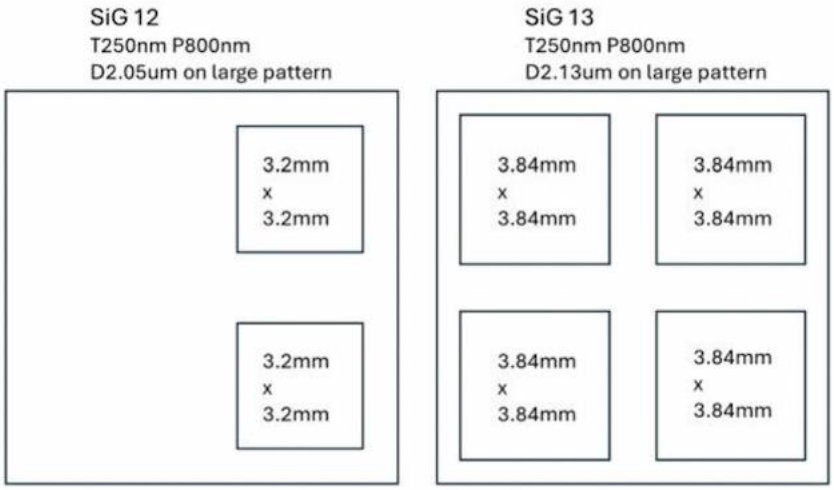

Figure 2.10. Diagram showing the layout of the silicon nanohole substrates. Both samples use identical nanohole parameters: diameter (T) of 250 nm and pitch (p) of 800 nm. The SiG 12 substrate (left) features two 3.2 mm x 3.2 mm patterned fields with a depth (D) of 2.05 µm. In contrast the SiG 13 substrate (right) consists of four 3.84 mm x 3.84 mm quadrants with an increased depth of 2.13 µm.

2.3.2 Soft Lithography

Using soft lithography, inverse replicas of the nanoholes were fabricated in NOA-81. The master Si nanohole substrate was partitioned into the 6 different designs via laser cutting. To optimize the polymer deposition process, two coating techniques were evaluated. Initial attempts using a spin-coater on old nanohole substrates resulted in the polymer layer fracturing during the removal process. Consequently, a different approach was undertaken where the polymer was poured manually on to the substrate, giving a more robust layer thickness.

To eliminate any trapped air, the NOA-81 coated substrates were put under vacuum. Within the timeframe given, we were only able to work with two substrates. One was put under vacuum for 3 hours and the other for 5 hours. Next, the substrates were put under a UV light source (UV-9W, 365 nm) for 7 minutes to cure the polymer. Finally, the NOA-81 polymer was lifted off the substrate using tweezers, leaving behind a negative reproduction of the initial silicon nanohole substrate.

2.4 Antimicrobial Surface Testing

2.4.1 Bacteria Preparation

E. coli ATCC 25992 was introduced to a blood agar plate from a ~80ºC frozen 7% DMSO stock and incubated for 24h at 37ºC. An isolated colony was picked from the blood agar plate and transferred to a tube with 10mL of tryptic soya broth (TSB, Oxoid, ref. CM0129) and incubated for 24h at 37ºC. Post-incubation the 10mL culture was transferred to 200mL TSB and incubated for 16-18h at 37ºC. The 200mL culture was then centrifuged at 5000g for 5 min at 10 ºC, the supernatant was decanted and resuspended in phosphate buffered saline (PBS),

these steps were repeated twice. Quantification of the bacteria was determined using a Bürker-Türk counting chamber (see Figure 2.11). The final suspension was diluted to a concentration of $1x10^7$ bacteria/mL in PBS with 1% v/v TSB.

Figure 2.11. Image of Bürker-Türk counting chamber.

2.4.2 Adhesion Experiment (2h) Colony Forming Units

The various surfaces were positioned into a 12-well plate and secured using double sided tape. A 2mL volume of the bacterial suspension was dispensed into each well and incubated for 2h at 37ºC. Every surface was cleaned once with 2mL PBS and transferred to a container with 2mL PBS and 0.1% v/v Tween 80, vortexed for 15 seconds and sonicated in a bath (Fisherbrand FB11203) for 5 min at ambient temperature (utilizing 37kHz and 100% power) to detach the bacteria from the surface. A 10-fold dilution series of the resulting suspension was prepared in PBS; 10µL of each dilution was inoculated in triplicate onto a TSB-agar plate (1.2% v/v agar BD, ref. 214530). After being allowed to air dry and post-incubation for 16-18h at 37ºC, the colony forming units (CFUs) were quantified.

2.4.3 Biofilm Experiment (24h) Colony Forming Units

The various surfaces were positioned into a 12-well plate and secured using double sided tape. A 2mL volume of the bacterial suspension was dispensed into each well and incubated for 2h at 37ºC. Following bacterial adhesion, the buffer was replaced with TSB medium and incubated for an additional 22h at 37ºC. Every surface was cleaned once with 2mL PBS and transferred to a container with 2mL PBS and 0.1% v/v Tween 80, vortexed for 15 seconds and sonicated in a bath (Fisherbrand FB11203) for 5 min at ambient temperature (utilizing 37kHz and 100% power) to detach the bacteria from the surface. A 10-fold dilution series of the resulting suspension was prepared in PBS; 10µL of each dilution was inoculated in triplicate onto a TSB-agar plate (1.2% v/v agar BD, ref. 214530) (see Figure 2.12). After being allowed to air dry and post-incubation for 16-18h at 37ºC, the CFUs were quantified.

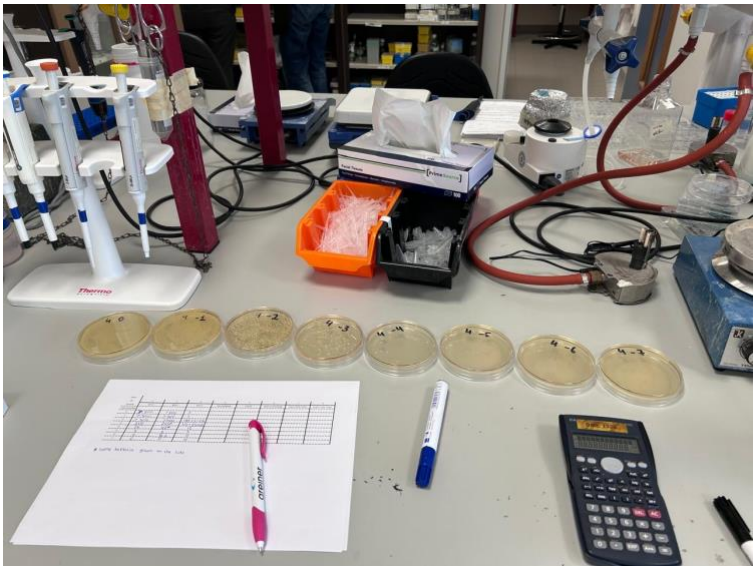

Figure 2.12. Image of the agar plates showing the results of serial dilutions.

2.4.4 Confocal Imaging

Plates were prepared following the adhesion and biofilm experiment for CFU, but instead the surfaces were incubated with a viability assay (LIVE/DEAD™ BacLight™ Bacterial Viability Kit, ref. L7012) (see section 1.2.3). For the 2h adhesion and 24h biofilm samples, incubation was carried out for 15 and 30 minutes, respectively, at ambient temperature in the dark. Following incubation, each surface was washed with 2 mL of PBS prior to imaging. The bacteria on the surfaces were visualised with a confocal laser scanning microscope (CLSM, Leica Stellaris 5), with a 40x water dipping objective (see Figure 2.13). Fluorescence parameters were set as follows:

- SYTO9 (shown as green): Excitation at 488 nm; emission recorded between 493-556 nm.
- PI (shown as red): Excitation at 561 nm and emission between 593-725 nm

Images were acquired at a resolution of 1024 x 1024 pixels, pinhole at 1, and a Z-stack of 50µm with 5 and 1 µm Z-steps for the 2h and 24h biofilm experiment respectively. Images were captured at 5 distinct fields per biological triplicate for the 2h adhesion experiment and 3 image stacks per triplicate for the 24h biofilm testing. Image analysis for the adhesion and biofilm experiments was carried out as follows:

- Adhesion (2h): Analysis was carried out using Fiji, by making a Z-stack overlay, and a threshold range of 50-200 was applied. The images were converted to a binary image and using the Analyse Particles plugin, particles between 5-200 pixels were counted as individual bacteria, with the automated counts validated through manual inspection.
- Biofilm (24h): Analysis was carried out using Comstat. A manual threshold at 80 was implemented, and the analysis for Biomass and Biomass Thickness were selected

Figure 2.13. Confocal Laser Scanning Microscope setup for the visualisation of E.coli.

2.4.5 Scanning Electron Microscope

Substrates were prepared as described in the adhesion and biofilm experiment, but instead the samples were dehydrated via an ascending ethanol series (10%, 25%, 40%, 50%, 70%, 80%, 90% and 96% v/v in demineralized water). Following this, the samples were dried in a desiccator until being used for SEM.

2.4.6 Statistical Analysis

Data was analysed using GraphPad Prism version 8 (Graphpad Software, La Jolla California USA). Initially, outliers were removed with a ROUT test set with a Q value at 1%. Subsequently, a One-Way analysis of variance (ANOVA) test with Tukey post hoc test was performed. Statistical differences were depicted with an asterisk with p-value ≤ *0.05, **0.01, ***0.001, ****0.0001). Normal distribution was assumed for all biological samples.

3. Results and Discussion

3.1 Overview of Fabricated Substrates

To evaluate the antimicrobial efficacy of various different topographies, five distinct substrate types were fabricated, as show in in Table 2. Both flat control surfaces and nanostructured surfaces were utilized to identify the optimal surface for inducing mechanical bacterial cell death.

Sample No.	Sample Name	Number of Samples Required	Fabrication Technique
1	Flat Silicon (control)	20	Purchased
2	Polymer Replica Samples*	20	Soft Lithography
3	Flat Polymer Surfaces (control)*	20	Soft Lithography
4	Black Diamond	20	30 mins HFCVD growth on Black Silicon Substrate
5	Flat Diamond (control)	20	6-hour HFCVD growth on Flat Silicon Wafer

Table 2. Comprehensive summary of fabricated substrates for antimicrobial testing. Asterisks (*) denote samples that were not completed within the experimental timeframe.

A total of 20 replicates were fabricated for each surface type to ensure statistical significance and to provide a contingency buffer due to unforeseen circumstances. Additionally, given the CVD chamber could accommodate a maximum of two bSi and six Si substrates per run, the seeding and deposition process was repeated several times to generate a total sample size of 20 for each substrate type. While the majority of the substrates were successfully prepared, the polymer-based samples (Samples 2 & 3) were not completed within the experimental timeframe. The fabricated samples were then sent to the University of Groningen in the Netherlands for antimicrobial testing.

The HFCVD parameters, specifically seeding and growth duration, were optimised based on the work done by previous students to achieve a uniform polycrystalline diamond coating. For the bD samples, a 30-minute growth was done to achieve a conformal coating down to the base of the nanostructures, while preserving the original shape of the underlying silicon nanostructures. Maintaining the sharpness of the nanostructure tips is critical for

mechanobactericidal activity; thus, growth times were strictly limited and precise to try to prevent rounding of the tips. Conversely, Flat-D growth required a 6-hour growth period to ensure a continuous, planar diamond film across the silicon wafer.

3.2 Diamond-Based Surfaces

bD surface analysis was conducted using SEM, Raman and WCA measurements to evaluate the fidelity of diamond growth, its chemical composition and surface chemistry respectively. It is worth mentioning that a visible change was observed after the HFCVD growth process, with a colour change from the initial black bSi substrate to a grey colour when bD was synthesised.

3.2.1 Scanning Electron Microscopy

SEM was used to analyse a variety of important features. This primarily included a focus on growth quality, nanopillar height, surface morphology.

Figure 3.1 presents the SEM micrographs obtained of the Flat-D surface at two magnifications with a continuous polycrystalline diamond film on the silicon surface. Although it is described as ‘flat’ diamond due to the absence of nanopillars, it is clear there is some surface roughness on the surface. At higher magnification (Figure 3.1(b)), the presence of randomly orientated diamond crystallites is observed. This intrinsic misorientation of the crystallites results in a root mean square (RMS) roughness of approximately 0.3 µm, demonstrating the microscopic topography is complex.[89] Importantly, the Flat-D surfaces demonstrate little to no antimicrobial behaviour, thus are used as a control for antimicrobial testing.

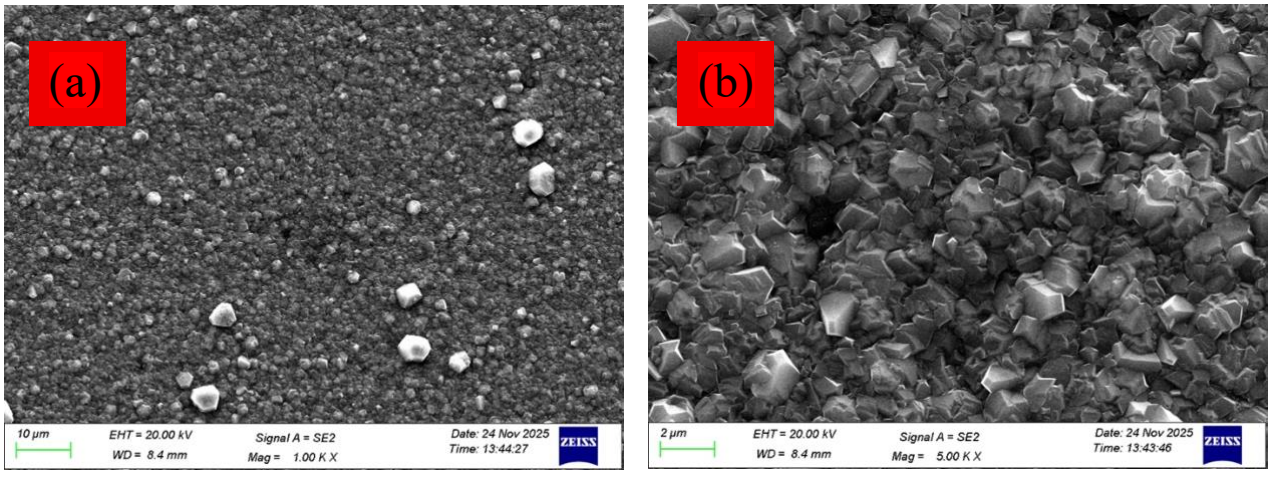

Figure 3.1. SEM images of flat diamond. (a) mag. x1000. (b) mag x5000.

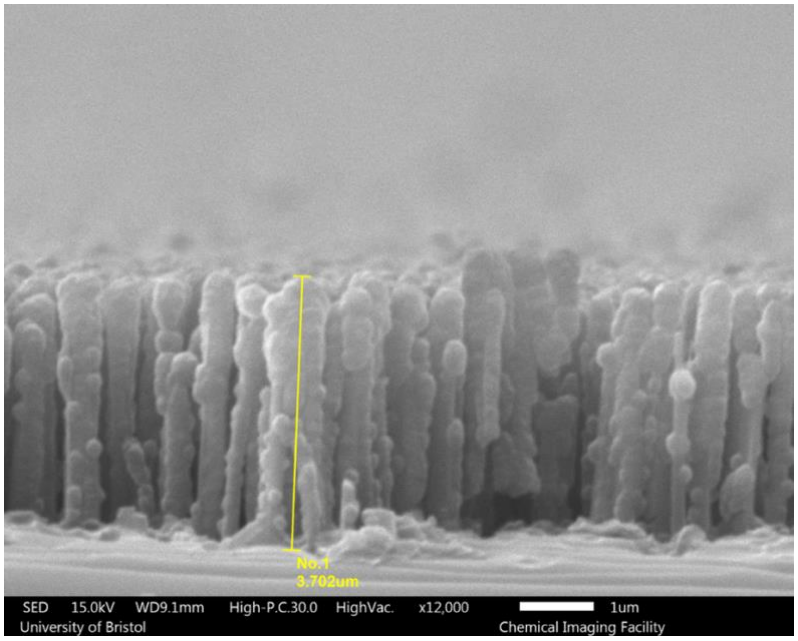

Figure 3.2. SEM image of black diamond with the pillar height quantified, mag. x12,000.

As shown in Figures 2.3, the SEM cross section demonstrates the successful conformal growth of polycrystalline diamond over the high-aspect-ratio silicon nanopillars. The resulting nanopillars achieved an average length of 3.702 μm, which aligns with heights reported in earlier studies (~3.0 μm) under identical 30-minute growth durations.[90]

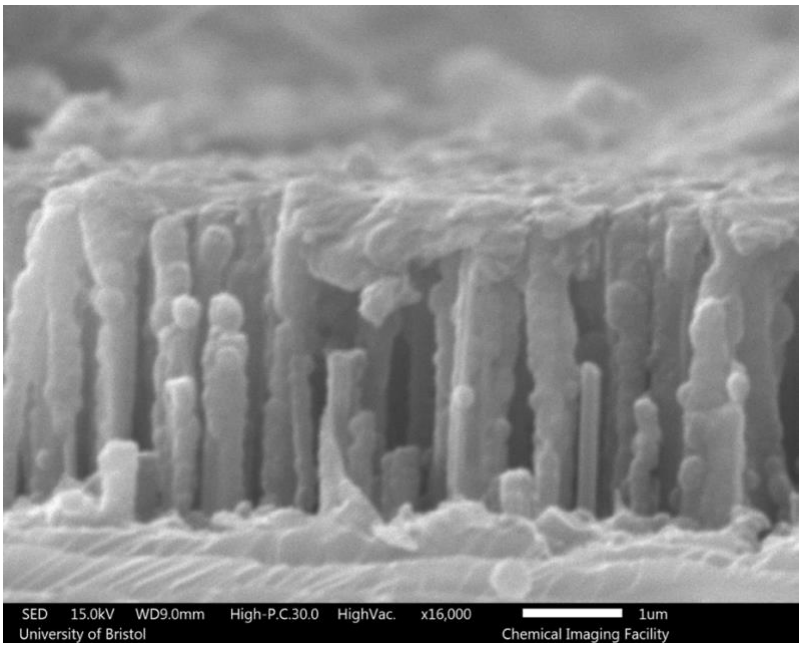

Figure 3.3. SEM image of black diamond, mag. x16,000.

However, the morphology was not uniform across the substrate. As seen in Figure 3.3, significant structural fracture was observed in isolated regions, highlighting the inherent mechanical fragility of the underlying bSi nanopillars. Furthermore, many nanopillars exhibited an overgrown and rounded tip and the presence of a thin, bridging diamond films. This transition from discrete needles to a semi-continuous film is due to overgrowth, where the accumulation of carbon species at the needle apexes reduces the sharpness of the physical piercing interface.

3.2.2 Raman Spectrum

The primary purpose of acquiring Raman spectra was to identify the chemical composition and quality of the diamond films grown on bSi and flat silicon.

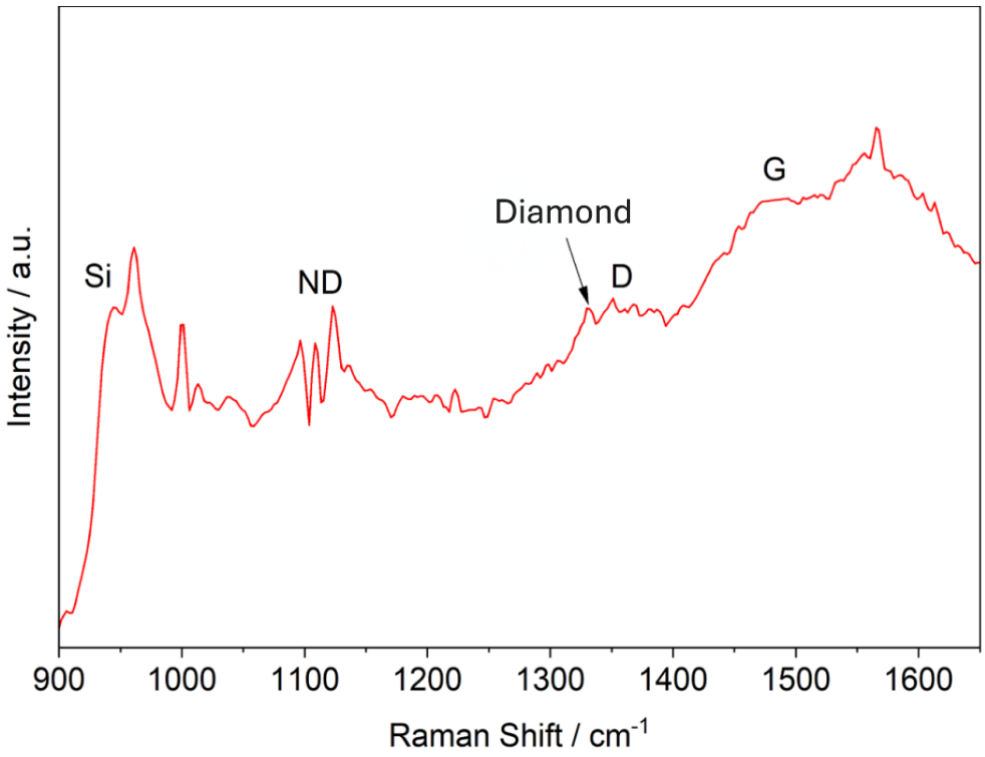

Figure 3.4. Raman spectrum of black diamond.

The measurements identified five distinct peaks located at 960 cm^{-1}, 1140 cm^{-1}, 1332 cm^{-1}, 1350 cm^{-1} and 1580 cm^{-1} in the spectra for bD (Figure 3.4). A relatively weak intensity peak for crystalline diamond is exhibited at 1332 cm^{-1}, as referenced in literature.[91] The substrates in this sample were fabricated with a thin polycrystalline layer of diamond, so it was anticipated that the relative intensity of the peaks would be weak. Given the 30-minute growth time on bSi, the resulting layer is thin and potentially non-contiguous. Consequently, a Si peak is shown which is due to the silicon core within these nanopillars. The spectral feature labelled 'ND' is

attributed to sp^2 carbon residing in the grain boundaries of nanodiamond materials. This is referred to as *trans*-polyacetylene.[92] The broad peaks between 1300 cm^{-1} and 1500 cm^{-1}, labelled 'D' and 'G' , are due to the presence of disordered sp^2 carbon and ordered graphitic clusters, respectively, arising from the sp^2 carbon species at the grain boundaries.

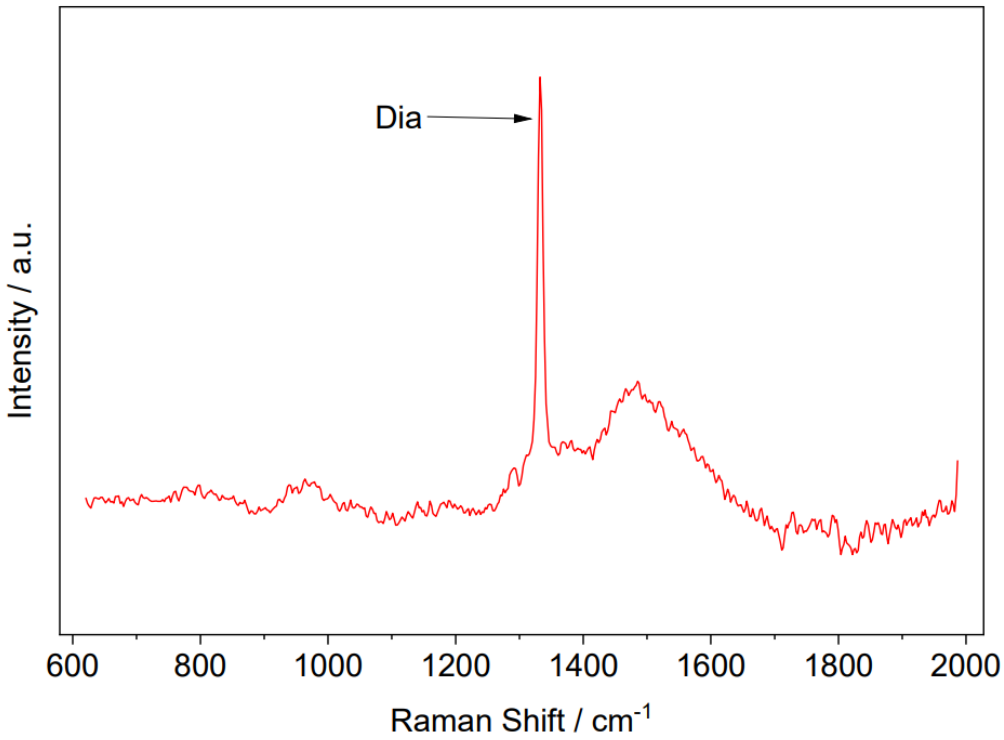

Figure 3.5. Raman spectrum of flat diamond.

The result of the Raman spectrum for Flat-D, shown in Figure 3.5, identifies the same distinct peaks as seen for bD. It is clear that the intensity of the diamond peak is stronger, indicative of a higher crystalline quality. There is a reduction in the intensity of the secondary features, again contributing to the increased quality of the diamond film.

3.2.3 Water Contact Angle Testing

To characterise the surface energy and wetting behaviour of the substrates to be tested, sessile drop WCA measurements were performed using a Kruss Droplet Shape Analyser. The results from this testing are essential in understanding how the chemical termination of the surfaces influence bacterial adhesion and biofilm formation.

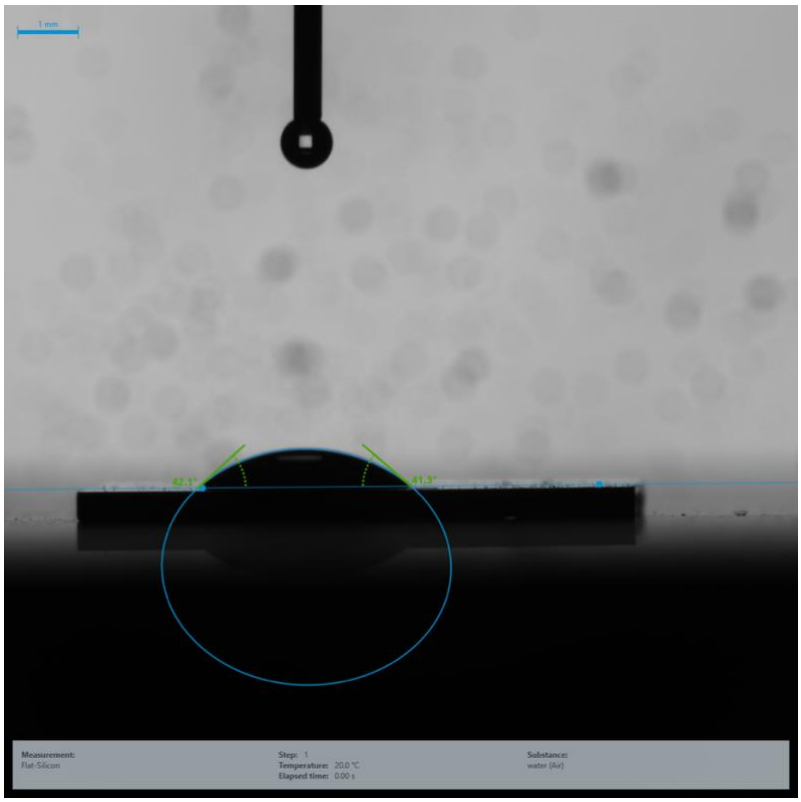

Figure 3.6. Flat silicon sessile drop contact angle.

Initial analysis of the control substrates established a baseline for hydrophilic and hydrophobic states. Flat silicon wafers exhibited a highly hydrophilic response with an average WCA of ~42° (Figure 3.6). This behaviour is primarily attributed to the development of a thick layer of silicon dioxide which tends to form quickly when exposed to air.[93]

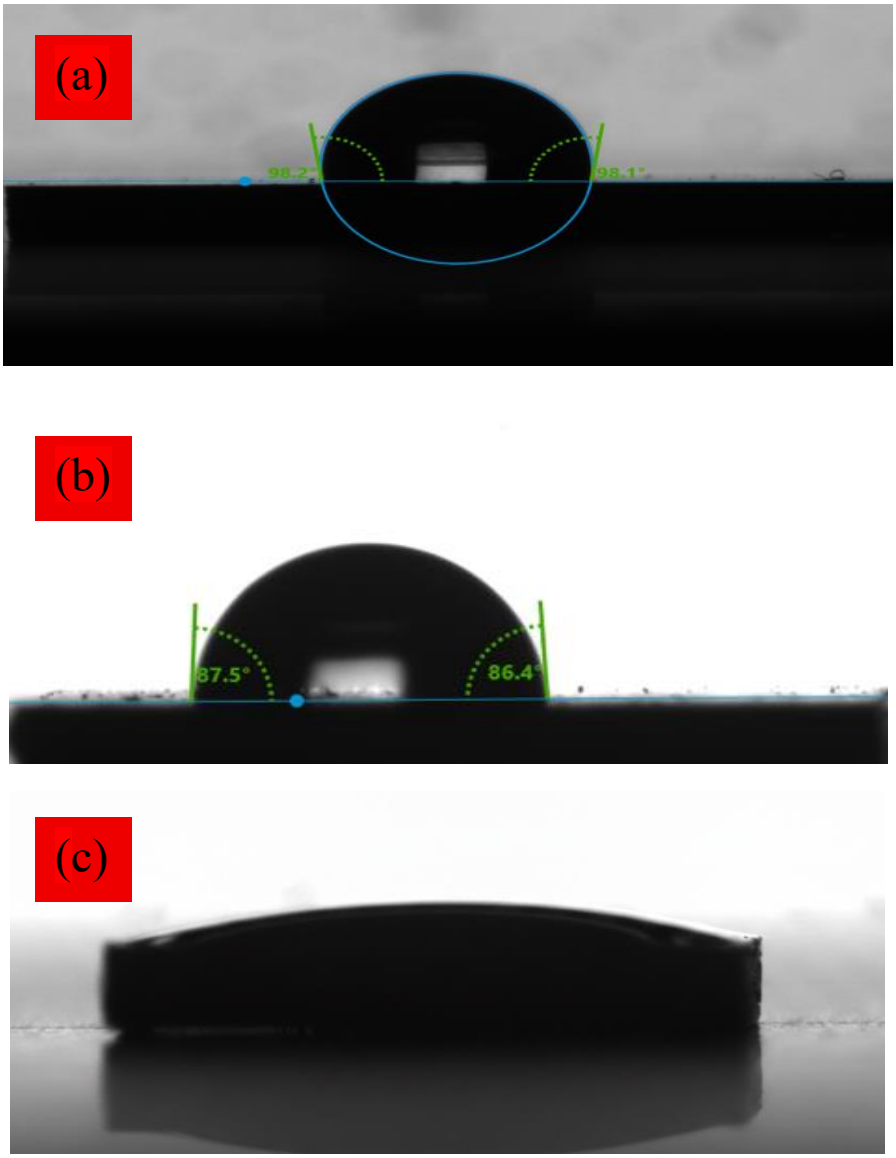

Figure 3.7. Representative images of the droplet profiles used to measure the contact angles for (a) H-terminated, (b) F-terminated, and (c) O-terminated Flat-D

In contrast, the H-terminated Flat-D surface demonstrated a hydrophobic surface, yielding an average WCA of ~98° (Figure 3.7(a)). This result is consistent with the H-terminated diamond films produced via HFCVD. Attempts were made to alter the surface chemistry of the diamond films to achieve varied wetting states. While fluorine termination is intended to induce a super-hydrophobic state (WCA > 150°), the WCA of fluorine-treated Flat-D samples yielded angles ~87° (Figure 3.7(b)). This indicates the fluorination process was unsuccessful, which is attributed to a malfunction in the DC plasma reactor. However, oxygen termination of Flat-D was successfully achieved, yielding angles <90°, demonstrating its hydrophilic character.

The surface behaviour of bD surfaces was further evaluated (Figure 3.8). The bD substrate yielded a WCA of 110.5°, representing an increase in hydrophobicity compared to Flat-D. This increase in the WCA illustrates the influence of the high-aspect-ratio nanopillars. According to

the Cassie-Baxter wetting model, air trapped within the interstitial gaps between the nanopillars reduces the effective solid-liquid contact area, thereby enhancing the hydrophobicity.[94] It should be noted that this measurement was performed on a sample that had aged for three weeks and was subsequently treated with TMCS to stabilise the surface energy. The use of TMCS was necessary to prevent the effect of atmospheric oxidation and contamination on the aged sample.

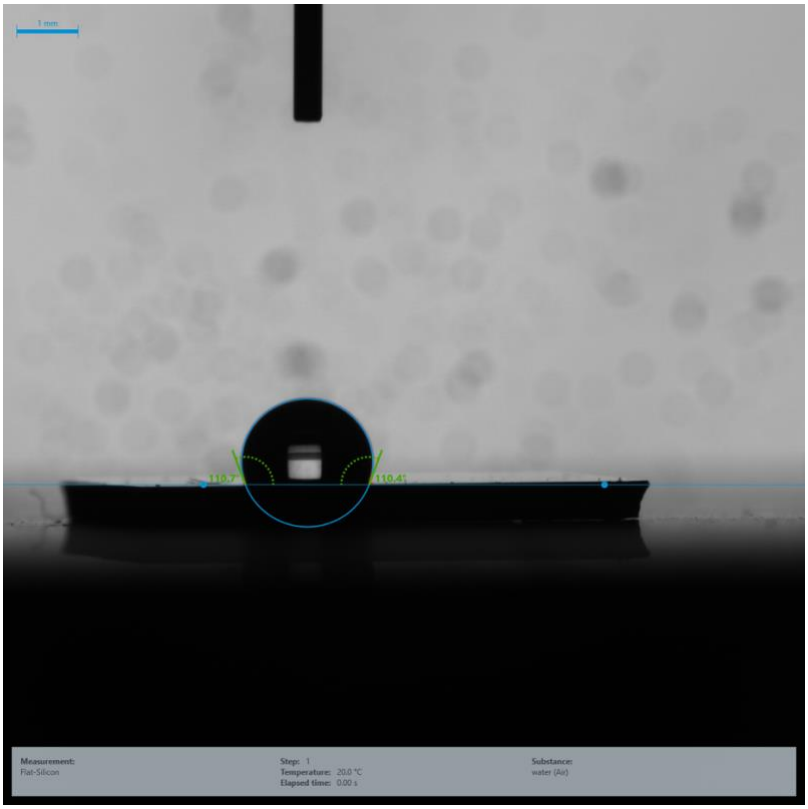

Figure 3.8. Black diamond sessile drop contact angle using TMCS.

3.2 Polymer Replication

The primary objective of this phase was to evaluate the fidelity of topographic replication from a fabricated Si nanohole into a polymer (NOA-81) matrix. SEM and LEXT analysis were employed to characterise the morphology of both the master template and the resulting polymer replicas.

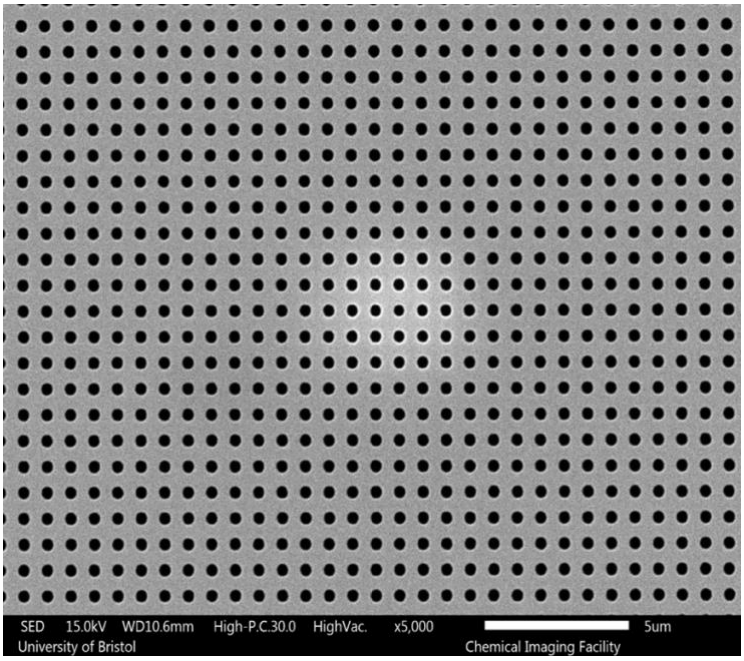

Figure 3.9. SEM image of fabricated Si nanohole substrate, mag. x5000.

The master substrate consisted of a fabricated 50x50 Si nanohole array as shown in Figure 3.9. The array possesses high periodic regularity with a consistent pitch, suggesting successful EBL and RIE of the silicon wafers. High-magnification analysis (Figure 3.10) reveals a nanohole diameter of ~290 nm, a pitch of ~820 nm and an inter-hole spacing of ~500 nm . These dimensions served as the benchmark for successful polymer infiltration and subsequent replication. Additionally, the LEXT profile in Figure 3.11 provide the third dimension. The holes have a depth of approximately ~2.0-3.0 µm.

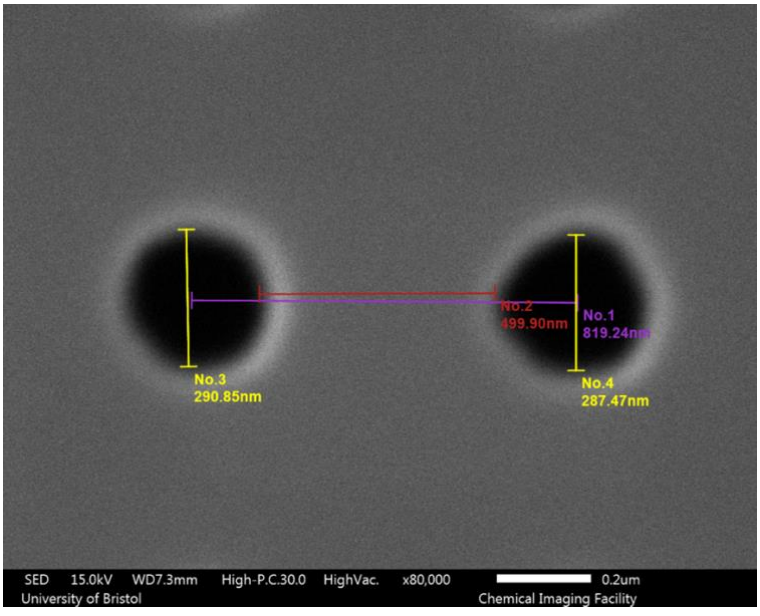

Figure 3.10. SEM image of Si nanohole substrate, mag. x80000.

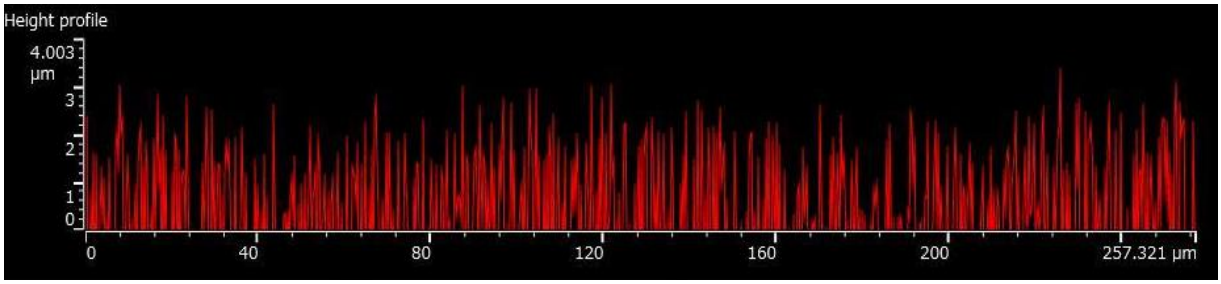

Figure 3.11. LEXT profile showing the depth of the nanoholes on the Si substrate.

Following the UV-curing process, the NOA-81 polymer was peeled from the Si nanohole substrate. As seen in Figure 3.12(a), the large-scale uniformity of the replication is evident, though some surface contaminants and bright replication are visible, likely representing areas where the polymer-substrate interface was compromised. Increasing the magnification to x2700 in Figure 3.12(b) allows for the clear distinction of individual nanopillars. These structures appear to have a high aspect ratio that corresponds well with the depth of the original Si nanoholes, confirming that the liquid polymer successfully reached the bottom of the template pores before solidification. The process was optimized from an initial trial run on an old substrate. It was discovered that applying a second polymer layer after the initial vacuum and UV-cure cycle significantly improved the ease of removal by increasing the structural integrity of the bulk polymer.

However, further analysis of different regions on the substrate reveals significant variations in structural stability. As seen in Figure 3.12(c), there is a distinct lack of vertical alignment. Instead of a uniform array of pillars, the surface is characterized by collapsed or flattened structures. This morphological failure is likely a result of mechanical distortion during the peeling process. As the polymer is peeled from the Si nanoholes, the high interfacial adhesion likely causes the needles to undergo plastic deformation, elongating and eventually collapsing onto the substrate surface.

Figure 3.13 shows the Si substrate following the removal of the polymer layer. The presence of residue is likely due to polymer that strongly adhered to the Si surface. This residue effectively prevented the formation of a continuous nanostructured array on the polymer surface. This indicates the need to incorporate anti-adhesive techniques for a higher-quality nanostructured polymer surface.

While these results indicate that NOA-81 is a viable polymer for biomimetic surface fabrication, it is important to note that due to time constraints, only a single replication cycle was completed during this study. Consequently, the observed results and structural collapse represent a preliminary result rather than an optimized output.

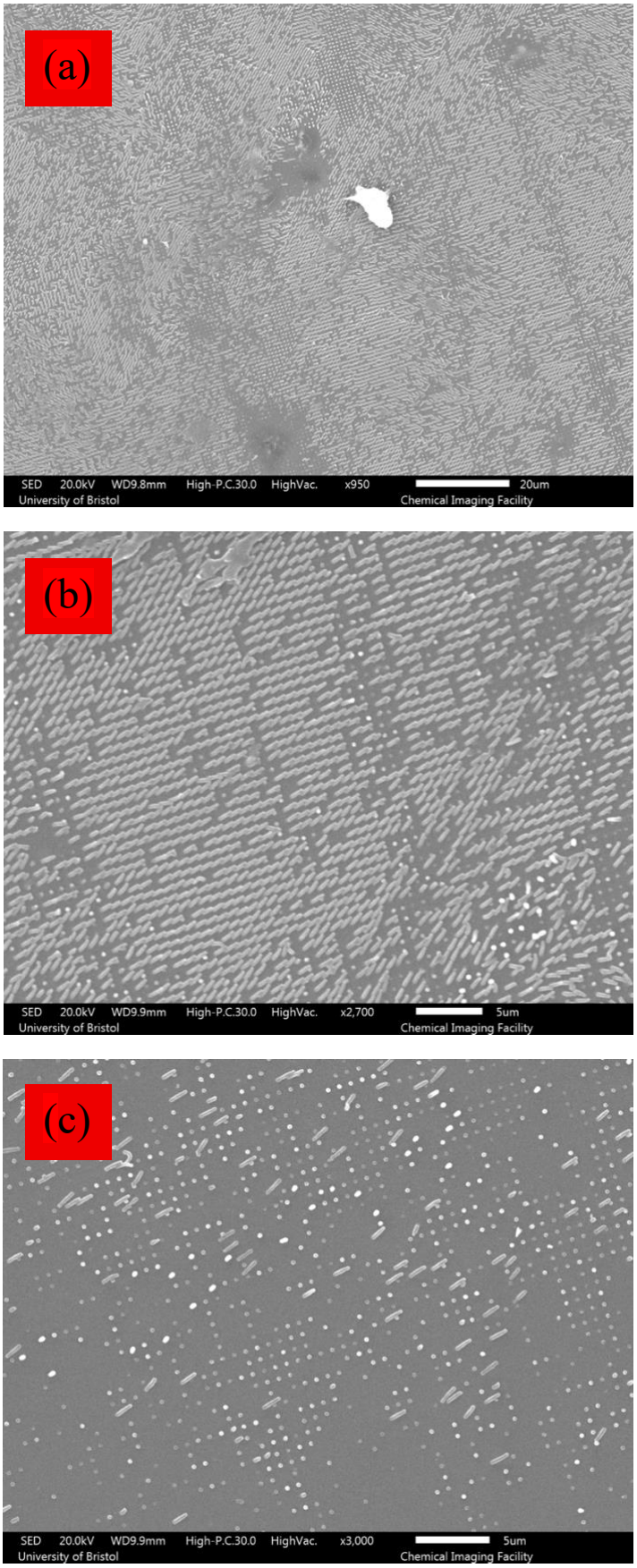

Figure 3.12. SEM images of nanostructured NOA-81 surface at various magnifications. (a) x950. (b) x2700. (c) x3000

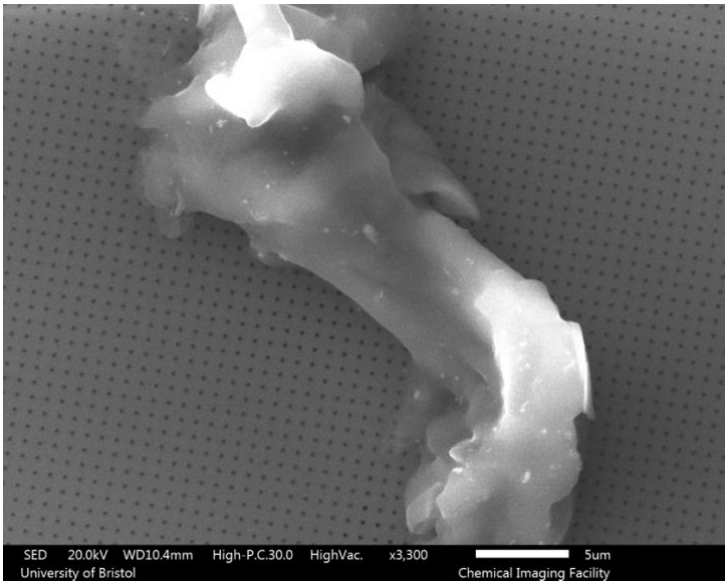

Figure 3.13. SEM image of Si nanohole substrate after polymer replication, mag. x3300.

3.3 Antimicrobial Testing

Surface	CFU/ cm^2
bD-H	1.07×10^7
bD-O	1.92×10^7
Flat-D-H	9.80×10^6
Flat-D-Polished	7.28×10^6
Flat-Si	3.51×10^7

Table 3. Table displaying the results of an E. coli CFU count assay, after 2 hours of incubation.

The initial CFU assay results for *E. coli* after 2 hours of incubation demonstrate the discrepancy in bacterial adhesion across the various fabricated surfaces. It is important to note that these are preliminary findings and full analysis of all 20 samples will be required for any statistical significance.

Results obtained from antimicrobial testing at the University of Groningen (Table 3 & Figure 3.14) indicate that all diamond-based surfaces, exhibited reduced bacterial adhesion compared

to the Flat-Si surface, regardless of their surface topography. This result has been demonstrated in existing research that indicate E. coli has an affinity for SiO_2, which as previously mentioned, spontaneously forms on silicon surfaces. This is likely driven by a conformational change in the outer membrane porins within the bacterial cell wall. Ultimately, this increases the membrane permeability of the cell wall and in turn facilitates an increased attachment to the substrate.[95]

The observation that H-terminated bD exhibits almost half the bacterial adhesion of O-terminated sample corroborates previous findings which suggest that a hydrophilic surface is less effective in inhibiting the adhesion of bacteria. This can be attributed to the Cassie-Baxter effect as it becomes increasing difficult for liquid to reach the base of the substrate between the nanopillars due to the presence of air in the gap thus reducing bacterial adhesion.[96]

Unexpectedly, the Flat-D samples resulted in the highest efficacy in inhibiting bacterial adhesion. One hypothesis is that perhaps instead of a mechanical piercing cell death mechanism, frequently associated with nanostructured surfaces, there could be an alternative anti-adhesive mechanism. However, further testing will be required to establish a conclusive result.

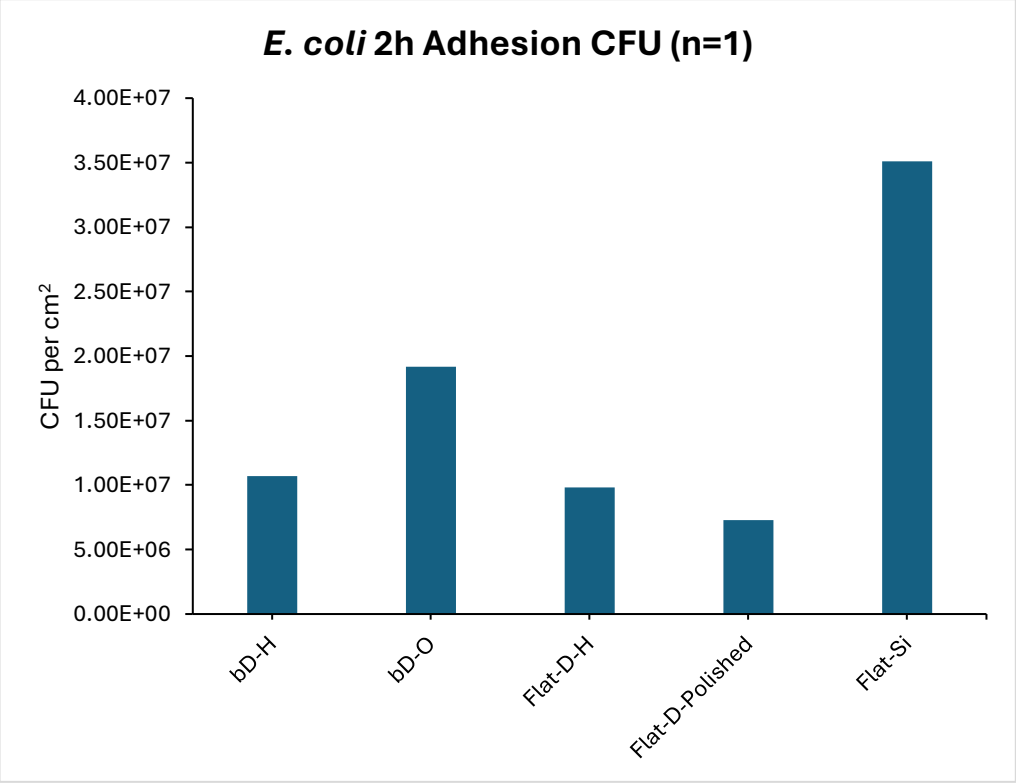

Figure 3.14. A graph displaying the results of an E. coli CFU count assay, after 2 hours of incubation.

4. Conclusion

This research project resulted in the successful fabrication of black diamond and flat diamond surfaces using HFCVD. Twenty replicas of each surface type were produced to be sent for antimicrobial testing at the University of Groningen in the Netherlands. The successful conformal growth of polycrystalline diamond over the high-aspect-ratio silicon nanopillars overcame the inherent fragility of the underlying silicon nanopillars. As the global threat of antimicrobial resistance continues to escalate, the outcomes of this work contribute to the necessary paradigm shift from chemical-based techniques to those based on mechanical bactericidal mechanisms inspired by biomimetic design.

The secondary objective established a novel proof-of-concept for a cost-effective fabrication polymer replication method using NOA-81 via soft lithography, which resulted in the successful fabrication of nanostructured surfaces from silicon nanohole templates. While structural collapse of the NOA-81 nanostructures was observed in isolated areas, likely due to interfacial adhesion during the peeling process, these findings show great promise. Given that time constraints restricted the lithography process to one replication, these findings provide a foundation for use of NOA-81 as a cost-effective alternative to black diamond.

Preliminary antimicrobial testing conducted at the University of Groningen provided initial findings into the antimicrobial activity of the fabricated surfaces against *Escherichia coli*. Results from a CFU assay indicated that all diamond-based surfaces exhibited reduced bacterial adhesion when compared to the Flat-Si surface, irrespective of their surface topography. Although the flat diamond control sample unexpectedly showed the highest efficacy in inhibiting bacterial adhesion, these results remain preliminary. Full analysis of the remaining samples is required to establish statistical significance and provide further insight into the mechanical cell lysis mechanism.

5. Future Work

To build upon this project, the immediate priority is the completion of experimental data from the University of Groningen. Evaluation using the results from the larger sample size of n=20 for each surface type is essential to establish statistical significance and provide definitive conclusions for future research pathways.

The soft lithography method requires further optimisation to ensure a perfect negative replication of the silicon nanohole substrate onto NOA-81. Future attempts should prioritise the inclusion of anti-adhesive agents or silanisation of the silicon nanohole template to prevent deformation of the surface during the peeling process. In particular, TMCS should be considered to coat the template prior to the polymer coating process. However, there remains a gap in the literature regarding how to reduce this interfacial adhesion. Finally, to validate the potential scalability of the NOA-81 method, a longevity study is necessary to assess its antimicrobial capacity.

In the long-term future, once an antimicrobial surface has demonstrated significant efficacy against bacteria in the 2h and 24h tests, further longitudinal studies will be required. As mentioned in Section 1.3.6, the accumulation of dead bacteria can mask the nanostructures. Future research would therefore benefit from the evaluation of a F-terminated surface, to support the current conclusion that hydrophobic surfaces demonstrate greater antimicrobial activity. F-terminated samples possess the greatest potential of self-cleaning properties, owing to their super-hydrophobicity. Additionally, dead bacteria could potentially attract more bacteria while also reducing the bactericidal efficacy of the nanopillars, so investigating this functionality represents a key future research direction to ensure the longevity of the antimicrobial surface. Consequently, the research times for all substrates should be extended from the 2h/24h period to a 7-day study to assess the long-term efficacy against bacteria and assess the accumulation of biofilm.

While this research focused on the Gram-negative *E. coli*., further antimicrobial testing must be conducted using Gram-positive bacteria, such as *S. aureus,* to validate the mechanical mechanism of the nanopillars. Due to the presence of the thick peptidoglycan wall, killing the cell via nanopillars becomes increasingly difficult. This would also provide further insight into the physical mechanism by which the nanopillars kill the cell.

6. References

1. M. Kolář, *Life (Basel)*, 2022, **12**, 468.
2. M. Naghavi et al., *The Lancet*, 2024, **404**, 1199–1226.
3. W. C. Reygaert, *AIMS Microbiol*, 2018, **4**, 482–501.
4. N. Malanovic and K. Lohner, *Biochimica et Biophysica Acta (BBA) - Biomembranes*, 2016, **1858**, 936–946.
5. A. A. Paray, M. Singh and M. Amin Mir, *Int J Res Rev*, 2023, **10**, 336–341.
6. M. Shehadul Islam, A. Aryasomayajula and P. R. Selvaganapathy, *Micromachines (Basel)*, 2017, **8**, 83.
7. A. Mathew, J. Hasan, S. Singamneni and P. K. D. V. Yarlagadda, *Advanced Engineering Materials*, 2023, **25**, 2201306.
8. C. Carrascosa, D. Raheem, F. Ramos, A. Saraiva and A. Raposo, *International Journal of Environmental Research and Public Health*, 2021, **18**, 2014.
9. P. Pereira-Silva, J. Borges and P. Sampaio, *Advances in Colloid and Interface Science*, 2025, **344**, 103590.
10. O. Grari, S. Ezrari, I. El Yandouzi, E. Benaissa, Y. Ben Lahlou, M. Lahmer, A. Saddari, M. Elouennass and A. Maleb, *The Microbe*, 2025, **8**, 100436.
11. K. Lewis, in *Bacterial Biofilms*, ed. T. Romeo, Springer, Berlin, Heidelberg, 2008, pp. 107–131.
12. S. Dhiman, A. Kumar, G. Kaur, G. Mukherjee, S. Rustagi, S. Shreaz, R. Negi and A. N. Yadav, *Biologia*, 2024, **79**, 3161–3181.
13. M. Elafify, X. Liao, J. Feng, J. Ahn and T. Ding, *Food Research International*, 2024, **190**, 114650.
14. Y. Hu, R. Li, K. Bian, Q. Zhou, Y. Pan, L. Ye, A. Li and P. Shi, *Water Research*, 2025, **268**, 122672.
15. Z. Xu, J. Wang, L. Xia and Y. Zhang, *International Journal of Thermal Sciences*, 2021, **161**, 106699.
16. N. Degiuli, I. Martić, C. G. Grlj and M. Zhang, *Energy Conversion and Management: X*, 2025, **28**, 101296.
17. M. A. Rather, K. Gupta and M. Mandal, *Braz J Microbiol*, 2021, **52**, 1701–1718.
18. I. Francolini, C. Vuotto, A. Piozzi and G. Donelli, *APMIS*, 2017, **125**, 392–417.
19. E. P. Ivanova et al., *Small*, 2012, **8**, 2489–2494.
20. E. P. Ivanova et al., *Small*, 2012, **8**, 2489–2494.
21. S. Pogodin et al., *Biophysical Journal*, 2013, **104**, 835–840.
22. K. Kashyap, A. Kumar, C.-N. Chen, M. Hou and J.-J. Yeh, 2014, pp. 648–651.
23. A. Velic, A. Jaggessar, T. Tesfamichael, Z. Li and P. K. D. V. Yarlagadda, *Nanomaterials*, 2021, **11**, 2472.
24. A. Velic, J. Hasan, Z. Li and P. K. D. V. Yarlagadda, *Biophys J*, 2021, **120**, 217–231.
25. S. M. Kelleher, O. Habimana, J. Lawler, B. O' Reilly, S. Daniels, E. Casey and A. Cowley, *ACS Appl Mater Interfaces*, 2016, **8**, 14966–14974.

26. Understanding ATP Bioluminescence in Food Safety, https://nextgenagrifoodsinsights.com/2025/03/07/understanding-atp-bioluminescence-in-food-safety-testing/, (accessed 5 February 2026).
27. J. Robertson, C. McGoverin, F. Vanholsbeeck and S. Swift, *Front Microbiol*, 2019, **10**, 801.
28. Bacterial Viability and Vitality Assays for Flow Cytometry - UK, https://www.thermofisher.com/uk/en/home/life-science/cell-analysis/flow-cytometry/flow-cytometry-assays-reagents/flow-cytometry-microbiology-assays/flow-cytometry-bacteria-viability-vitality-assays.html, (accessed 29 January 2026).
29. P. Pereira-Silva, J. Borges and P. Sampaio, *Advances in Colloid and Interface Science*, 2025, **344**, 103590.
30. H. Dollwet and J. Sorenson, *Trace elements in medicine*, 1985, 80–87.
31. S. Mathews, M. Hans, F. Mücklich and M. Solioz, *Appl Environ Microbiol*, 2013, **79**, 2605–2611.
32. S. I. Choi, M. S. Chang, T. Kim, K. H. Chung, S. Bae, S.-H. Kim, C. J. Yoon, Y. K. Kim and J. H. Woo, *Korean J Intern Med*, 2021, **36**, 1204–1210.
33. J. O. Noyce, H. Michels and C. W. Keevil, *Applied and Environmental Microbiology*, 2006, **72**, 4239–4244.
34. S. L. Warnes and C. W. Keevil, *PLOS ONE*, 2013, **8**, e75017.
35. S. Ali, A. Bahadur, A. Hassan, S. Ahmad, W. Shah and S. Iqbal, *Chemical Engineering Journal*, 2025, **507**, 160470.
36. S. E. Jin and H.-E. Jin, *Nanomaterials (Basel)*, 2021, **11**, 263.
37. L. F. A. A. Raj, A. Annushrie and S. K. R. Namasivayam, *The Microbe*, 2025, **7**, 100331.
38. J. Šístková, T. Fialová, E. Svoboda, K. Varmužová, M. Uher, K. Číhalová, J. Přibyl, A. Dlouhý and M. Pávková Goldbergová, *Sci Rep*, 2024, **14**, 17303.
39. A. Shea and M. T. Bernards, *Molecules*, 2025, **30**, 2710.
40. U. E. and S. N. Lindh, Nobel Prize-awarded material that puncture and kill bacteria, https://www.chalmers.se/current/news/life-nobel-prize-awarded-material-that-puncture-and-kill-bacteria/, (accessed 5 February 2026).
41. Z. Cao, S. Pandit, F. M. A. Noa, J. Zhang, W. Gao, S. Rahimi, L. Öhrström and I. Mijakovic, *Advanced Science*, 2025, **12**, e05976.
42. F. Atteia, J. Le Rouzo, L. Denaix, D. Duché, G. Berginc, J. J. Simon and L. Escoubas, *Materials Research Bulletin*, 2020, **131**, 110973.
43. Z. Zhao, Z. Zhang, J. Jing, R. Gao, Z. Liao, W. Zhang, G. Liu, Y. Wang, K. Wang and C. Xue, *APL Mater.*, 2023, **11**, 021107.
44. J. Y.-H. Chai, B. T. Wong and S. Juodkazis, *Materials Today Energy*, 2020, **18**, 100539.
45. APL Materials, https://pubs.aip.org/apm, (accessed 6 February 2026).
46. J.-H. Park, L. Gu, G. von Maltzahn, E. Ruoslahti, S. N. Bhatia and M. J. Sailor, *Nat Mater*, 2009, **8**, 331–336.
47. P. K. Agnihotri, V. Ghai and H. Singh, *Sci Rep*, 2018, **8**, 12312.
48. N. Norouzi, W. Woudstra, E. J. W. Smith, G. Zulpukarova, K. Yao, V. G. Damle, R. Schirhagl, P. W. May and T. Kamp, *Adv Eng Mater*, 2023, **25**, 2301031.

49. P. W. May et al., *J. Mater. Chem. B*, 2016, **4**, 5737–5746.
50. N. Norouzi, W. Woudstra, E. J. W. Smith, G. Zulpukarova, K. Yao, V. G. Damle, R. Schirhagl, P. W. May and T. Kamp, *Adv Eng Mater*, 2023, **25**, 2301031.
51. P. Arunachalhalam, in *Polymer-based Nanocomposites for Energy and Environmental Applications*, Woodhead Publishing, 2018, pp. 315–332.
52. S. Cui, K. Sun, Z. Liao, Q. Zhou, L. Jin, C. Jin, J. Hu, K.-S. Wen, S. Liu and S. Zhou, *Science Bulletin*, 2024, **69**, 2080–2088.
53. L. M. Cox, A. M. Martinez, A. K. Blevins, N. Sowan, Y. Ding and C. N. Bowman, *Nano Today*, 2020, **31**, 100838.
54. N. Unno and T. Mäkelä, *Nanomaterials*, 2023, **13**, 2031.
55. Z. Alnakhli, Z. Liu, F. AlQatari, H. Cao and X. Li, *Nanoscale Advances*, 2024, **6**, 2954–2967.
56. J. O. Carneiro, V. Teixeira, P. Carvalho, S. Azevedo and N. Mannine, 2011, p. 448.
57. D. Ikkene, O. M. Eggenberger, C.-A. Schoenenberger and C. G. Palivan, *Current Opinion in Colloid & Interface Science*, 2023, **66**, 101706.
58. T. Turcitu, C. J. K. Armstrong, N. Lee-Yow, M. Salame, A. V. Le and M. Fenech, *Micromachines*, 2023, **14**, 2033.
59. E. Berthier, E. W. K. Young and D. Beebe, *Lab Chip*, 2012, **12**, 1224–1237.
60. F. Pereira Sales, R. Ariati, V. Noronha[1] and J. Ribeiro, *Procedia Structural Integrity*, 2022, **37**, 383–388.
61. A. H. Abdul Manap, S. S. Md Izah and K. Mohamed, *ACS Omega*, 2019, **4**, 20257–20264.
62. P. Wägli, A. Homsy and N. Rooij, *Procedia Engineering*, 2010, **5**, 460–463.
63. R. Li, X. Lv, M. Hasan, J. Xu, Y. Xu, X. Zhang, K. Qin, J. Wang, D. Zhou and Y. Deng, *J Chromatogr Sci*, 2016, **54**, 523–530.
64. S. Rezvani, N. Shi, T. M. Squires and C. F. Schmidt, *J. Phys. D: Appl. Phys.*, 2018, **51**, 045403.
65. S. Wu, F. Zuber, K. Maniura-Weber, J. Brugger and Q. Ren, *J Nanobiotechnology*, 2018, **16**, 20.
66. M. Dickson, E. Liang, L. Rodriguez, N. Vollereaux and A. Yee, *Biointerphases*, 2015, **10**, 021010.
67. D. P. Linklater, S. Saita, T. Murata, T. Yanagishita, C. Dekiwadia, R. J. Crawford, H. Masuda, H. Kusaka and E. P. Ivanova, *ACS Appl. Nano Mater.*, 2022, **5**, 2578–2591.
68. M. Day, M. Pamato, D. Novella and F. Nestola, *La Rivista del Nuovo Cimento*, DOI:10.1007/s40766-023-00045-6.
69. The History of Diamonds, https://www.blackacreldn.com/journal/white-diamonds, (accessed 6 February 2026).
70. Network Covalent Atomic Solids- Carbon and Silicates, https://chem.libretexts.org/Courses/Pasadena_City_College/CHEM_001A%3A_General_Chemistry_and_Chemical_Analysis/13%3A_Solids_and_Modern_Materials/13.06%3A_Network_Covalent_Atomic_Solids-_Carbon_and_Silicates, (accessed 6 February 2026).
71. A. Rifai, S. Houshyar and K. Fox, *Annals of 3D Printed Medicine*, 2021, **1**, 100002.

72. A. Fiorani and Y. Einaga, *ACS Electrochem.*, 2025, **1**, 1983–2013.
73. First-ever diamond sola, https://www.ecoticias.com/en/first-diamond-solar-cell-in-history/13456/, (accessed 9 February 2026).
74. S. Irina, M. Polikarpov and A. Snigirev, *Synchrotron Radiation News*, 2022, **34**, 12–20.
75. C. Chen and Q. CHEN, *International Journal of Modern Physics B*, 2008, **22**, 309–326.
76. M. Jiang, C. Chen, P. Wang, D. Guo, S. Han, X. Li, S. Lu and X. Hu, *Proceedings of the National Academy of Sciences*, 2022, **119**, e2201451119.
77. P. W. May, *Philos Trans A Math Phys Eng Sci*, 2000, **358**, 473–495.
78. S. Luzhao, G. Yuan, L. Gao, J. Yang, M. Chhowalla, M. H. Gharahcheshmeh, K. K. Gleason, Y. S. Choi, B. H. Hong and Z. Liu, *Nature Reviews Methods Primers*, DOI:10.1038/s43586-020-00005-y.
79. S. Matsumoto, Y. Sato, M. Tsutsumi and N. Setaka, *J Mater Sci*, 1982, **17**, 3106–3112.
80. L. Schäfer, M. Höfer and R. Kröger, *Thin Solid Films*, 2006, **515**, 1017–1024.
81. A. Kausar, *Materials Research Innovations*, 2018, **22**, 302–314.
82. A. Peethan, M. Aravind and S. D. George, *Advances in Superhydrophobic Coatings*, 2023, 1-25.
83. O. Dunseath, E. J. W. Smith, T. Al-Jeda, J. A. Smith, S. King, P. W. May, A. H. Nobbs, G. Hazell, C. C. Welch and B. Su, *Sci Rep*, 2019, **9**, 8815.
84. Z. Xie, P. Zhang, Z. Zhang, C. Chen and X. Wang, *Chinese Chemical Letters*, 2024, **35**, 109768.
85. G. Zulpukarova, unpublished work.
86. M. Page, MSci, University of Bristol, 2023.
87. H. Liu and D. S. Dandy, *Diamond Chemical Vapor Deposition*, DOI:10.1016/B978-081551380-3.50004-9.
88. LEXT OLS5100 Laser Microscope, https://evidentscientific.com/en/products/digital-imaging/lext-ols5100, (accessed 15 April 2026).
89. M. J. Romeu, L. C. Gomes, R. Teixeira-Santos, G. Zulpukarova, W. Woudstra, J. Atema-Smit, G. Geertsema-Doornbusch, R. Schirhagl, P. W. May and F. J. Mergulhão, *Environmental Research*, 2026, **299**, 124321.
90. G. Hazell, P. W. May, P. Taylor, A. H. Nobbs, C. C. Welch and B. Su, *Biomater. Sci.*, 2018, **6**, 1424–1432.
91. M. G. Donato, G. Faggio, M. Marinelli, G. Messina, E. Milani, A. Paoletti, S. Santangelo, A. Tucciarone and G. Verona Rinati, *Diamond and Related Materials*, 2001, **10**, 1788–1793.
92. R. Pfeiffer, H. Kuzmany, P. Knoll, S. Bokova, N. Salk and B. Günther, *Diamond and Related Materials*, 2003, **12**, 268–271.
93. P. Bryk, E. Korczeniewski, G. S. Szymański, P. Kowalczyk, K. Terpiłowski and A. P. Terzyk, *Materials (Basel)*, 2020, **13**, 1554.
94. A. B. D. Cassie and S. Baxter, *Trans. Faraday Soc.*, 1944, **40**, 546–551.
95. R. Lozins, T. Selga and D. Ozoliņš, *Heliyon*, 2020, **6**, e03678.
96. J. Xu, X. Zhang, J. Dai, D. Yu, M. Ji and M. Chen, *Journal of Materials Research and Technology*, 2023, **23**, 1360–1374.